

REVIEW

Open Access



# Planar metasurface-based concentrators for solar energy harvest: from theory to engineering

Cheng Zhang<sup>1,2</sup>, Yujie Zhan<sup>2</sup>, Yongxue Qiu<sup>2</sup>, Leilei Xu<sup>2</sup> and Jianguo Guan<sup>2\*</sup> 

\*Correspondence:  
guanjg@whut.edu.cn

<sup>1</sup> Hubei Engineering Research Center of RF-Microwave Technology and Application, School of Science, Wuhan University of Technology, Wuhan 430070, China

<sup>2</sup> State Key Lab of Advanced Technology for Materials Synthesis and Processing, International School of Materials Science and Engineering, Wuhan University of Technology, Wuhan 430070, China

## Abstract

Solar energy is an inexhaustible renewable energy resource, which is a potential solution to global warming and aids sustainable development. The use of solar-thermal collectors to harness solar energy facilitates low-cost heat storage and can improve the stability of power grids based on renewable energy. In solar-thermal collectors, traditional concentrators, such as parabolic troughs and dishes, are typically used but inevitably require high-precise supports and complex tracking sun systems, which increase the cost of solar-thermal power stations and hinder their further applications. In contrast, planar meta-lenses (so-called metasurface-based concentrators) consisting of two-dimensional nanostructured arrays are allowed to engineer the frequency dispersion and angular dispersion of the incident light through delicately arranging the aperture phase distribution, thereby correcting their inherent aberrations. Accordingly, the novel meta-lenses offer tremendous potentials to effectively capture broadband, wide-angle sunlight without the extra tracking system. This review summarizes the research motivation, design principles, building materials, and large-area fabrication methods of meta-lens for solar energy harvesting in terms of focusing efficiency, operation bandwidth, and angular dependence. In addition, the main challenges and future goals are examined.

**Keywords:** Solar-thermal collector, Metasurface, Concentrator, Solar energy harvesting

## Introduction

Global energy consumption reached 2.9% in 2018 and is continuing to rapidly increase [1]. Fossil fuels (coal, crude oil, natural gas, etc.) are the mainstream sources of energy in modern societies. However, known reserves are likely to substantially deplete in the next one hundred years. Moreover, there are well-documented associated environmental concerns related to their usage [2–4]. Renewable energy sources such as bioenergy, biomass, wind, sunlight, tide, and hydrogen [5–9] have attracted widespread attention owing to their environmental friendliness and inexhaustibility. Among them, the use of solar-thermal energy precedes that of any other renewable energy technologies, and can be traced back to several centuries BC in terms of the lighting of fires for various purposes, e.g., lighting the Olympic torch, wars and performances in Mesopotamia, ancient

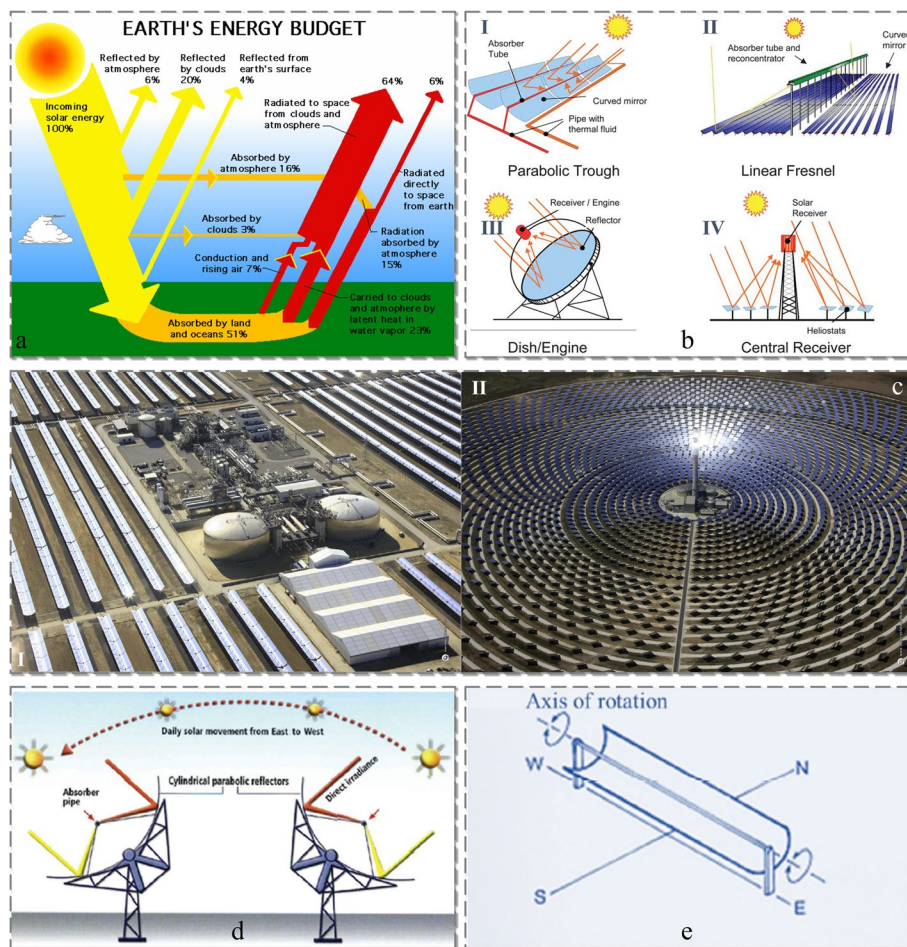


**Fig. 1** (a) Energy budget of the solar energy that is incident on the Earth's surface (from NASA sources). (b) Schematic of different concentrating solar systems: (I) Parabolic trough solar collector; (II) Linear Fresnel reflector; (III) Parabolic dish; (IV) Solar tower. (c) (I) Solar field of SENERtrough® cylindrical-parabolic collectors. Aerosol and Termesol thermosolar plants, owned by Torresol Energy. c(II) Gemasolar thermosolar plant, owned by Torresol Energy and developed by SENER. Tracking mechanisms for parabolic trough solar collector: (d) East-west tracking and (e) north-south tracking. (a) Reproduced with permission [13]. Copyright 2013, Elsevier. (b) Reproduced with permission [14]. Copyright 2012, Royal Society of Chemistry. (c) Reproduced with permission [15]. Copyright 2017, Elsevier. (d) Reproduced with permission [16]. Copyright 2017, Elsevier. (e) Reproduced with permission [17]. Copyright 2011, Elsevier

Greek and Roman with the help of burning glass (namely primitive lens) technology [10–12]. In addition, solar energy is still the most abundant renewable energy resource that is available on Earth, except for the dual dissipation owing to the atmosphere and clouds, as shown in Fig. 1(a). According to data published by the World Radiation Centre, the solar energy incident on the outer atmosphere of Earth is  $1367 \text{ W/m}^2$  with 1% uncertainty. Only 0.1% of this irradiance value can generate four times the entire world consumption capacity, even at an efficiency of 10% [18]. Thus, solar energy is a promising solution to the global energy crisis.

Concentrated solar power (CSP) systems [15, 19–21] are required to continuously harness the solar energy that penetrates through the Earth's atmosphere with high efficiency. Using this scheme, solar radiation is concentrated over a point or

line-shaped solar-thermal collector to produce high-temperature thermal energy for applications such as heating [17, 22–27], thermal energy storage [13, 28–30], and the production of electricity [31, 32]. Owing to their economic feasibility and broad compatibility with other traditional or renewable energy sources, it is predicted that CSP plants will supply up to 7% of global electricity demand by 2030, and potentially 25% by 2050 [33].

Depending on the adopted focusing strategy, CSP systems can be classified into two categories: line focusing types including parabolic trough solar collectors [16, 34–36] (Fig. 1b(I)) and linear Fresnel reflectors [37, 38] (Fig. 1b(II)), and point-focusing type that utilize a parabolic dish [14, 20, 39–42] (Fig. 1b(III)), which include the solar tower [43–45] (Fig. 1b(IV)). These lenses and reflectors continuously modulate the propagation phase of solar radiation according to their refraction indices and spatial locations. Each of them has different capabilities in terms of temperature range, cost, efficiency, etc. For example, parabolic trough collectors (Fig. 1c(I)) and solar towers (Fig. 1c(II)) are convenient options for electricity generation due to their low operating cost, high efficiency, and flexibility of scaling in large power plants [14, 46]. In a CSP system, a one-axis (parabolic trough) or two-axis (linear Fresnel reflector, solar tower, and parabolic dish) with a sun tracking system (as shown in Fig. 1(d–e)) typically utilize lenses and mirrors to ensure that the incident solar radiation is perpendicular to the reflection apertures throughout the daytime, so that the radiant energy can be effectively collected. This leads to extra complexity and higher cost.

Alternatively, optical metasurfaces [47–56] have planar structures consisting of building blocks (also called artificial meta-atoms) at subwavelength scales. They exhibit unusual abilities to manipulate electromagnetic waves on-demand, thereby offering a fundamentally new method for generating discrete phase profiles via strong coupling between building blocks and incident waves. Optical meta-lenses, namely metasurface-based concentrators, exhibit great potential to achieve considerable angle dispersion and frequency dispersion through designing the building blocks. Thus, they are expected to replace traditional lenses and mirrors to efficiently capture broadband, wide-angle sunlight without the need for tracking sun systems to generate cost-effective electricity by exploiting spatially distributed solar energy. In addition, they are more suitable for the development of compact platforms than the curved lenses or mirrors used in CSP systems.

Over the past few years, metasurfaces have been utilized for various fascinating applications, such as in beam-shaping devices [47, 57–60] (Fig. 2(a)), holographic imaging [61, 65–68] (Fig. 2(b)), polarization converters [69–72], surface wave couplers [62, 73–77] (Fig. 2(c)), meta-lenses [63, 78–81] (Fig. 2(d)), and reconfigurable meta-devices [64, 82–87] (Fig. 2(e)), wherein specific dispersive properties are required. Meta-lenses are among the most commonly explored meta-optical devices, driven by applications in microscopy and imaging [88]. They have facilitated the development of revolutionary tools to modulate the scattering patterns in near or far fields. Recently, planar meta-lenses have been adopted in augmented reality and virtual reality (VR) optics, due to their extremely thin profiles compared to conventional optical elements [89–94]. Although meta-lenses have been widely investigated in a variety of optical

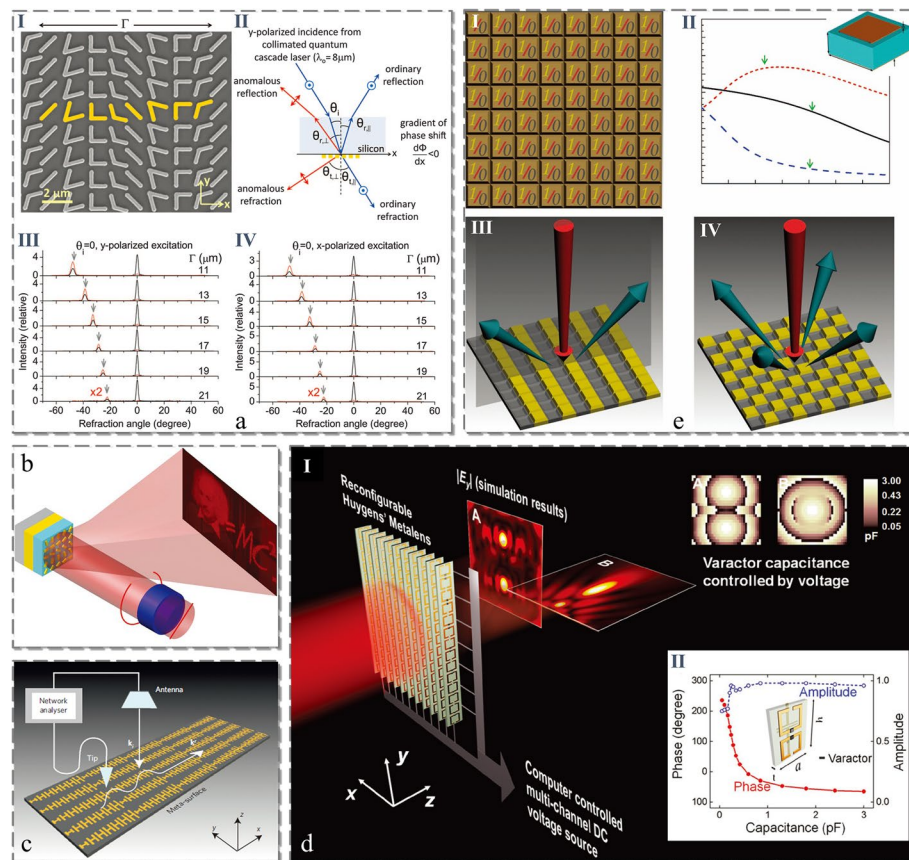


**Fig. 2** (a) Light propagation with phase discontinuities: (I) Scanning electron microscope (SEM) image of a representative antenna array. (II) Schematic experimental setup for y-polarized excitation (electric field normal to the plane of incidence); (III and IV) Measured far-field intensity profiles of the refracted beams for y- and x-polarized excitations. (b) Illustration of a reflective nanorod-based computer-generated hologram for a circularly polarized incident beam. (c) Schematic description of a specific gradient index metasurface that can convert a propagating wave into a surface wave with nearly 100% efficiency. (d) Reconfigurable Huygens' meta-lens and characteristics of meta-atom: (I) Active Huygens' meta-lens for dynamic electromagnetic wave focusing. Upper-right inset: spatial distribution of the capacitances used to achieve two focal spots; (II) Capacitance-dependent phase and amplitude responses of electromagnetic wave transmission for incident electric and magnetic fields. (e) 1-bit digital metasurface and coding metasurface: (I) 1-bit digital metasurface composed of only two types of elements: '0' and '1'; (II) A square metallic patch unit structure (inset) to realize '0' and '1' elements and the corresponding phase responses; (III and IV) Two 1-bit periodic coding metasurfaces for controlling the scattering of beams. (a) Reproduced with permission [47]. Copyright 2011, American Association for the Advancement of Science. (b) Reproduced with permission [61]. Copyright 2015, Nature Publication Group (NPG). (c) Reproduced with permission [62]. Copyright 2012, NPG. (d) Reproduced with permission [63]. Copyright 2017, Wiley-VCH. (e) Reproduced with permission [64]. Copyright 2014, NPG

systems, there is no review systematically discussing them regarding solar energy collection so far.

This review presents a summary of current research and the main challenges associated with the use of meta-lenses to capture sunlight to the best of our knowledge. It is organized as follows: After briefly introducing the state-of-the-art and significance of solar energy concentration in Section 1, we present the design fundamentals of a meta-lens in Section 2. Then, the three key factors (including focusing efficiency, operation bandwidth, and angular stability) that directly impact the performance of solar concentrators are fully discussed in Section 3 to Section 5, respectively. Section 6 introduces the

fabrication method for large-area all-dielectric meta-lenses before the conclusion and outlook of meta-lenses for solar-thermal energy harvesting are given in the end.

### Design principles and physical mechanisms

To design a flat meta-lens with desired features, three factors including the full-phase meta-atom design, arrangement of the target phase profile, and building material selection, must be carefully considered.

The target phase profile is generally calculated using either ray tracing or a Fourier-optics method to implement various special functions such as aberration correction, high-efficient focus, and a large numerical aperture (NA) at a selected wavelength. To focus planar incident light at an arbitrary target point, the typical distribution of phase retardation of a meta-lens is calculated as follows:

$$\varphi(\rho, \lambda_0) = -\left[2\pi \left(\sqrt{\rho^2 + f^2} - f\right)\right] / \lambda_0 \quad (1)$$

where  $\rho$  is given by  $\sqrt{x_0^2 + y_0^2}$ , which represents the distance from the arbitrary position  $(x_0, y_0)$  to the predefined origin of the coordinates on the plane of the meta-lens,  $f$  is the focal length (FL), and  $\lambda_0$  is the operation wavelength. The phase profile is similar to that of a series of concentric circles for an aperture with a decreasing phase delay from the projection location of the focal spot to the edge of the meta-lens.

To introduce a predesigned phase profile based on a calculation using Eq. (1), the phase modulation introduced by the meta-atoms should cover the full phase from 0 to  $2\pi$  [47, 95]. A full-phase response can be achieved either by resonant or non-resonant effects, as shown in Fig. 3(a), or a combination of both [96]. The resonant effects that can generate a sufficient phase shift typically include localized resonances (Mie resonances [97, 101, 102] shown in Fig. 3(b), Fabry-Perot resonances [72, 103–107], and plasmonic resonances [98, 108, 109] illustrated in Fig. 3(c)) and extended resonances (photonic crystals [99, 110–112] in Fig. 3(d) and high-contrast gratings [113–115]). Owing to its multi-pass property, the resonant strategy tends to exhibit a relatively low aspect ratio (AR), which yields several advantages for sample fabrication and reproducibility. However, the intrinsically narrow operating bandwidth and sensitive manufacture tolerance lead to limitations in their practical applications.

The non-resonant strategy can control the phase shift of the wavefronts that interact with the nanostructures by adjusting the effective refractive index, which is determined by the periodicity, diameter, and height of the meta-atoms at a subwavelength scale (Fig. 3(e)), or by exploiting the geometric phase (Fig. 3(f)). The former propagation phase is stimulated by waveguides or waveguide-like modes without polarization selection [100, 116–118] and can be derived as [119]

$$\varphi = \frac{2\pi}{\lambda_0} n_{eff} H \quad (2)$$

where  $n_{eff}$  is the effective refractive index, and  $H$  is the height of the basic blocks. To achieve  $2\pi$  phase coverage between unit cells with maximum and minimum filling factors, the height of the meta-atom should satisfy the following condition:

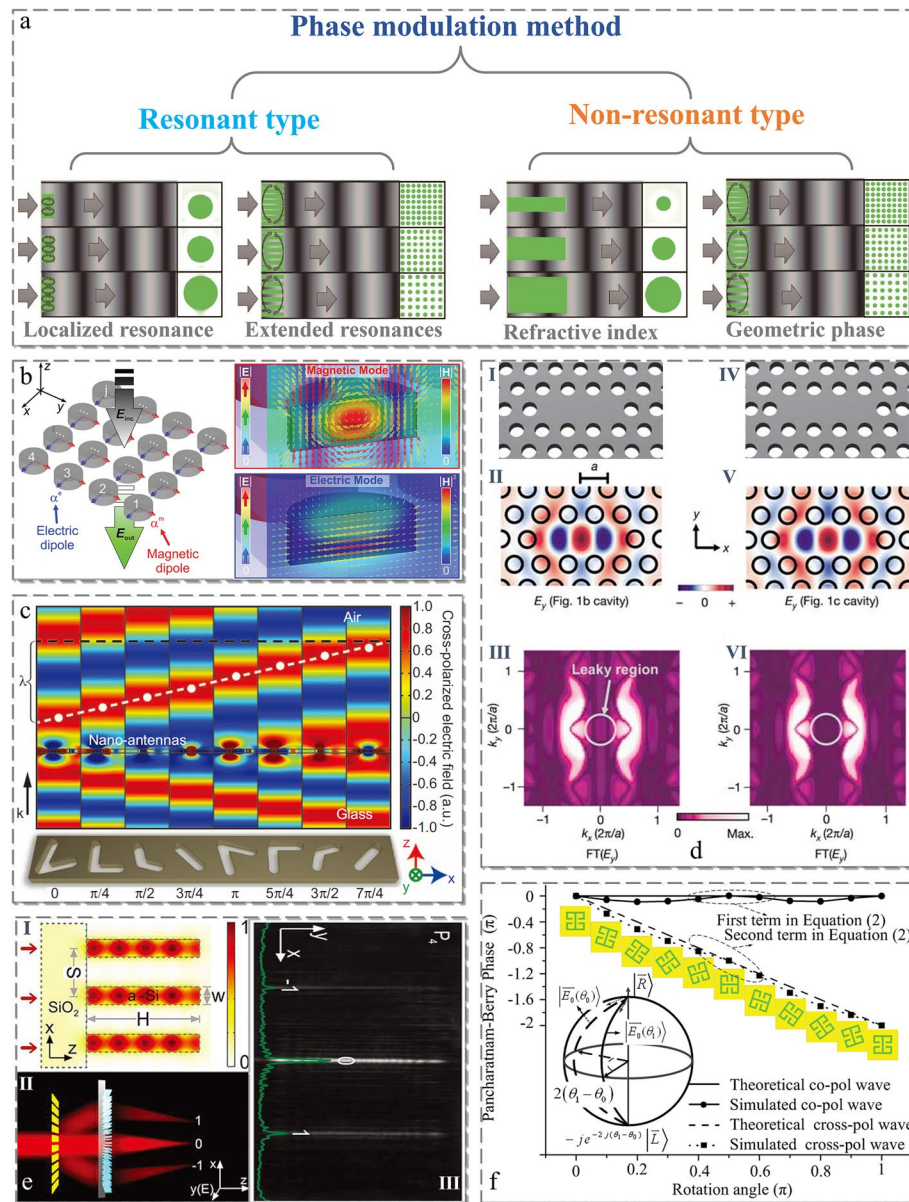


**Fig. 3** (a) High-level schematic of various of nanostructures to achieve phase control in metasurfaces. (b) Schematic of Mie resonant: an (infinite) array of nanodisks represented as electric and magnetic dipoles with polarizabilities  $a^e$  and  $a^m$  for  $x$ -polarized incident light. Electric (colored arrows) and magnetic (plain color-coded) field distributions of the magnetic (right-top) and electric (right-bottom) mode of a silicon (Si)-nanodisk metasurface. (c) Schematic designs and the results of full-wave simulations of the individual Babinet-inverted nanoantennas. The pseudo-color field map indicates the cross-polarized light scattered from each nano-antenna. (d) Photonic nanocavities using a two-dimensional (2D) photonic-crystal slab: (I) Starting cavity structure with three missing air rods (I) and designed cavity structure created by displacing the air rods at both edges (IV); (II and III) and (V and VI) Electric field profile and 2D Fourier transform spectrum, respectively, for the designed cavity shown in (I) and (IV). (e) Schematic of the Fourier meta-lens (I) and magnetic intensity distribution of the dielectric waveguide (II). Intensity distribution in the focal plane (III). (f) PB geometric phase variation of the co-polarization (solid lines) and cross-polarization (dashed lines) transmitted wave, as a function of the orientation angle of the unit cell. The inset shows a visualization of the PB phase on the Poincaré sphere. (a) Reproduced with permission [96]. Copyright 2019, Optical Society of America (OSA). (b) Reproduced with permission [97]. Copyright 2015, Wiley-VCH. (c) Reproduced with permission [98]. Copyright 2013, NPG. (d) Reproduced with permission [99]. Copyright 2003, NPG. (e) Reproduced with permission [100]. Copyright 2018, Wiley-VCH. (f) Reproduced with permission [69]. Copyright 2015, Wiley-VCH

$$H = \frac{\lambda_0}{n-1} \quad (3)$$

where  $n$  is the refractive index of the building material. Once the material is decided, the dimension along the transmission direction is essentially fixed, resulting in the enhancement of the optical frequency. In addition, the corresponding profile is significantly elevated, setting a stricter requirement for the processing technology.

The latter method, known as Pancharatnam-Berry (PB) phase modulation [69, 120–122], must be triggered by circularly polarized incident light, and the corresponding phase responses are positive relative to the rotation angle of the nanofins or nanopillars. The Jones matrix can be used to describe the geometric phase modulation, and thus, an anisotropic unit cell with a space-varying fast axis can be expressed as [123, 124]

$$T = M(-\theta) \begin{bmatrix} t_x & 0 \\ 0 & t_y \end{bmatrix} M(\theta) \quad (4)$$

$$R = M(-\theta) \begin{bmatrix} r_x & 0 \\ 0 & r_y \end{bmatrix} M(\theta) \quad (5)$$

where  $t_x/r_x$  and  $t_y/r_y$  are the transmission/reflection coefficients of the linearly polarized incident light along the long and short axes of the nanofins or nanopillars, respectively.  $M(\theta)$  denotes a rotation matrix  $\begin{bmatrix} \cos \theta & -\sin \theta \\ \sin \theta & \cos \theta \end{bmatrix}$ . When exposed to circularly polarized light, using the Jones matrix, the transmitted/reflected electric field from anisotropic meta-atoms can be described as follows:

$$\begin{bmatrix} E_{tx} \\ E_{ty} \end{bmatrix} = \frac{t_x + t_y}{2} \begin{bmatrix} 1 \\ \pm i \end{bmatrix} + \frac{t_x - t_y}{2} \exp(\pm i2\theta) \begin{bmatrix} 1 \\ \mp i \end{bmatrix} \quad (6)$$

$$\begin{bmatrix} E_{rx} \\ E_{ry} \end{bmatrix} = \frac{r_x + r_y}{2} \begin{bmatrix} 1 \\ \pm i \end{bmatrix} + \frac{r_x - r_y}{2} \exp(\pm i2\theta) \begin{bmatrix} 1 \\ \mp i \end{bmatrix} \quad (7)$$

Equation (6) and (7) show that the output electric fields consist of two orthogonal circular polarizations (CPs). The second term on the right side of Eq. (6) and (7) implies that the transmitted or reflected light acquires an opposite-handedness and is simultaneously phase-shifted by  $\arg\left(\frac{t_x/r_x - t_y/r_y}{2}\right) \pm 2\theta$ . Thus, when the nanofins or nanopillars rotate by  $\theta$ , a phase delay of  $\pm 2\theta$  is realized considering the different spin states. Therefore, the geometric phase can cover the entire  $2\pi$  range when an anisotropic nanostructure is rotated from 0 to  $\pi$ . Note that the sign of the additional phase  $\pm 2\theta$  depends on the incident CP states (incident light with left-handed CP has a positive phase, but a negative phase is added to the right-handed circular waves). Furthermore, with the further development of meta-theory, high-order geometric phases equal to multiple times the rotation angle ( $\pm 3\theta$ ,  $\pm 4\theta$ ...) have been achieved using meta-atoms with high fold rotational symmetries [125]. Unlike the resonant phase modulation methods, the geometric phase is not sensitive to the incident wavelength, and therefore is convenient for broadband performance. However, the polarized-sensitive PB structures typically

require a higher AR than resonant scatters because of the limited refractive index of the building materials [126].

In addition, a detour phase modulation strategy has also been reported to control the propagation phase along a different direction from the incident one [127, 128]. The principle of the detour phase modulation is shown in Fig. 4(a) [129]. When a light shines on two adjacent meta-atoms, it will be diffracted and produce a second wave of identical phase. With regard to the diffraction wave at a fixed refraction angle  $\theta$ , the corresponding phase difference  $\Delta\phi$  can be derived as

$$\Delta\phi = 2\pi D \sin \theta / \lambda \quad (8)$$

Therefore, the required full-phase response is achieved by continuously changing the distance  $D$  between the meta-atoms without considering the polarization state and incident angle. Due to these natural advantages, the detour phase is used widely in holographic imaging, beam shaping (Fig. 4(b)), optical signal processing, and others [130–133], but seldomly for meta-lens design because of the relatively low energy distribution at the high order diffraction.

Finally, for the building materials selection, plasmonic metals (e.g., Al, Ag, Au, etc.) in early research were widely used for meta-lens design, but their ohmic losses significantly degrade performance at optical frequencies [57, 79, 98, 108, 134–141]. For instance, Pors et al. proposed a reflection-type broadband focusing flat mirror in the near-infrared (NIR) regime. The metal-insulator-metal configuration was adopted to realize a hyperboloidal phase profile, in which the top metal layer consisted of a subwavelength periodic arrangement of nanobricks with different sizes [79]. The designed structure has been fabricated and characterized, and its broadband-focusing properties have been confirmed. However, at a wavelength of 800 nm and an FL of  $\sim 12 \mu\text{m}$ , an efficiency of merely 30% was achieved. Compared to its microwave and terahertz counterparts [70, 139], such an optical meta-lens has a relatively low efficiency, which is mainly due to fabrication errors and material losses. A transmission-type plasmonic meta-lens consisting of complementary Babinet-inverted nanoantennas was demonstrated by Ni et al. to focus the transmission of the NIR energy [98]. The nanovoids allow for discrete phase shifts ranging from 0 to  $2\pi$  for cross-polarized scattered light, and therefore, focusing at a distance of only 2.5 mm

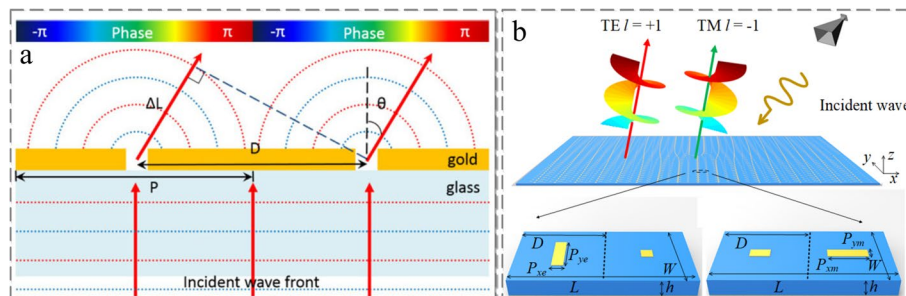


**Fig. 4** **a** Principle of the detour phase. **b** Schematic of the detour phase metasurface for dual-polarized vortex beam generation. **a** Reproduced with permission [129]. Copyright 2016, Wiley-VCH. **b** Reproduced with permission [130]. Copyright 2022, IEEE



was experimentally achieved using a 4 mm diameter meta-lens for light with a wavelength of 676 nm by utilizing predesigned meta-atoms. Although this type of meta-lens is extremely small (just a few micrometers in diameter) and thin (much smaller than the wavelength), the focusing efficiency of plasmonic meta-lenses is minimal due to the inevitable ohmic losses at high frequencies. Considering the difficulty in improving the focusing ability by employing metal materials, dielectric materials that can drastically increase focal efficiency have attracted much attention in recent years. Furthermore, these materials are naturally more compatible with complementary metal-oxide-semiconductor technologies [142–144]. In particular, dielectric-resonance/non-resonance-based optical meta-lenses exhibit numerous advantages compared to their metallic counterparts.

Given that the refractive index and loss characteristic exhibit frequency dispersions, the common materials for building optical metasurfaces are summarized based on their operation wavelengths. For example, niobium pentoxide ( $\text{Nb}_2\text{O}_5$ ) [145], hafnium oxide ( $\text{HfO}_2$ ) [146, 147], and aluminum nitride (AlN) [148, 149] are utilized for the ultraviolet (UV) band; titanium dioxide ( $\text{TiO}_2$ ) [119, 150–155], silicon nitride ( $\text{Si}_3\text{N}_4$ ) or silicon-rich nitride ( $\text{SiN}_x$ ) [156–159], crystalline silicon (*c*-Si) [160–162], and gallium nitride (GaN) [163–165] are candidates for the visible regime; germanium (Ge) [166, 167], poly-silicon (*p*-Si) [114, 142], amorphous silicon (*a*-Si) [168–172], and lead telluride (PbTe) [173, 174] are suitable for infrared (IR) wavelengths.

### Focusing efficiency

The efficiency of a meta-lens is key to its application in a solar-thermal system. To construct a high-efficiency meta-lens, the ideal building materials require a low absorption coefficient, high refractive index, and ease of manufacture. From Fig. 5(a), the solar radiation covers the ultra-broad bandwidths from the NIR region (from 780 nm to 2526 nm) to the deep-UV (DUV) range (from 190 nm to 280 nm) [18, 176, 177]. According to the

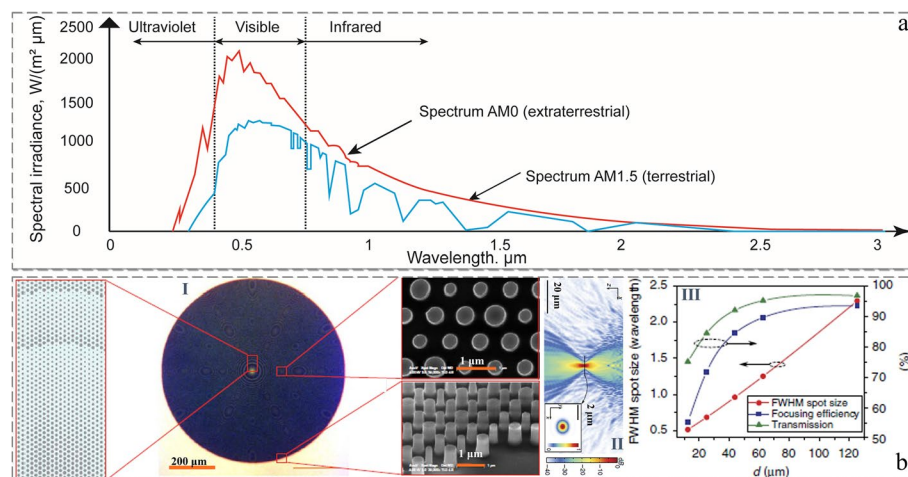


**Fig. 5** (a) Conceptual depiction of the spectrum of solar irradiance, i.e., the power density of solar radiation as a function of wavelength. (b) Schematic of the aperiodic HCTA lens (left panel of b(I)), optical microscopy image of a fabricated HCTA lens (middle panel of b(I)), and SEM images (right panel of b(I)) of the Si posts that form the HCTA lens. b(II) Logarithmic scale electric energy density at the plane of focus. b(III) Measured plane of focus FWHM spot size, transmission, and focusing efficiency of the HCTA micro-lens as a function of focusing distance. (a) Reproduced with permission [18]. Copyright 2021, published by Springer Nature. (b) Reproduced with permission [175]. Copyright 2015, NPG

aforementioned introduction of the building materials, a meta-lens that is formed using different materials generally operates at the corresponding spectrum, and thereby, we will introduce the high-focusing-efficiency optical meta-lenses in terms of their working wavelengths, including the NIR [169, 174, 178–182], visible [134, 152, 164, 165, 183–187], and UV bands [146, 148, 149, 188–193]. The focusing efficiency is defined as the optical power confined within a focal spot divided by the corresponding incident power.

### NIR wavelengths

*a*-Si has both a high refractive index and mature nanofabrication technology, and is the best candidate in the NIR range. By utilizing this element, Arbabi et al. reported on a linear-polarization (LP)-insensitive, micron-thick ( $0.038\lambda_0$ ), high-contrast transmit array (HCTA) micro-lens (Fig. 5b(I)). The hexagonal lattice (top-right of Fig. 5b(I)) consisted of different *a*-Si circular posts that were specially designed as the basic nanoblock to realize a large transmittance (more than 92%), and their phase could be tuned from 0 to near  $2\pi$  using the propagation phase induced by truncation waveguide modes [175]. Based on careful structural adjustment, the optimum phase masks that were fabricated in one lithographic step could focus 1550 nm light from a single-mode fiber to the smallest diffraction-limited spots (Fig. 5b(II)) with an efficiency of up to 82% (Fig. 5b(III)). Kenney et al. demonstrated meta-lenses that operated at 1064 nm, with a 1 mm aperture and four different FLs (0.5 mm, 1.0 mm, 2.0 mm, and 5.0 mm). The meta-lenses were composed of *a*-Si pillars with a height of 700 nm with a diameter ranging from 70 nm to 360 nm, which were fabricated using electron-beam lithography (EBL) and reactive ion etching (RIE), on top of a fused-silica ( $\text{SiO}_2$ ) substrate [194]. The focusing efficiency of the fabricated meta-lens was measured up to 67%. Furthermore, large-area meta-lenses with 10 mm apertures for which the number of pillars per meta-lens exceeds 550 million have been designed and manufactured by utilizing an efficient Python script in 14 hours using EBL. However, because of intrinsic ohmic losses, the performance of *p*-Si, *a*-Si, or PbTe deteriorates substantially in the visible to UV regions. In contrast, *c*-Si,  $\text{TiO}_2$ , and GaN have been utilized to improve the focusing efficiency in the visible range.

### Visible light region

Liang et al. proposed an ultrahigh NA (1.48 for experiment and 1.73 for simulation) high transmittance meta-lens in the visible range (Fig. 6a(I)), based on *c*-Si, which has a higher refractive index than that of  $\text{TiO}_2$  and GaN. This facilitates the further increase of the NA [160]. By utilizing the geometric phase approach that was realized using nanobricks on a sapphire film (Fig. 6a(II)) in an arrangement determined using a hybrid optimization algorithm, the meta-lens was operated in the air (left side and middle side of Fig. 6a(III)) with a full width at half maximum (FWHM) of 277 nm (right side of Fig. 6a(III)), and the focusing efficiency reached 67% at 532 nm wavelength. The corresponding FWHM can be reduced to 207 nm (right side of Fig. 6a(IV)) when the meta-lens is immersed in oil with a refractive index of 1.512 (left side and middle side of Fig. 6a(IV)). Phan et al. introduced a strategy for optimizing the focusing efficiency of a meta-lens in a computationally efficient manner [195]. By stitching together individually optimized apertures, a large-area, high-NA *c*-Si meta-lens with focusing efficiencies exceeding 90% was demonstrated at 640 nm when illuminated with linearly polarized electromagnetic radiation.

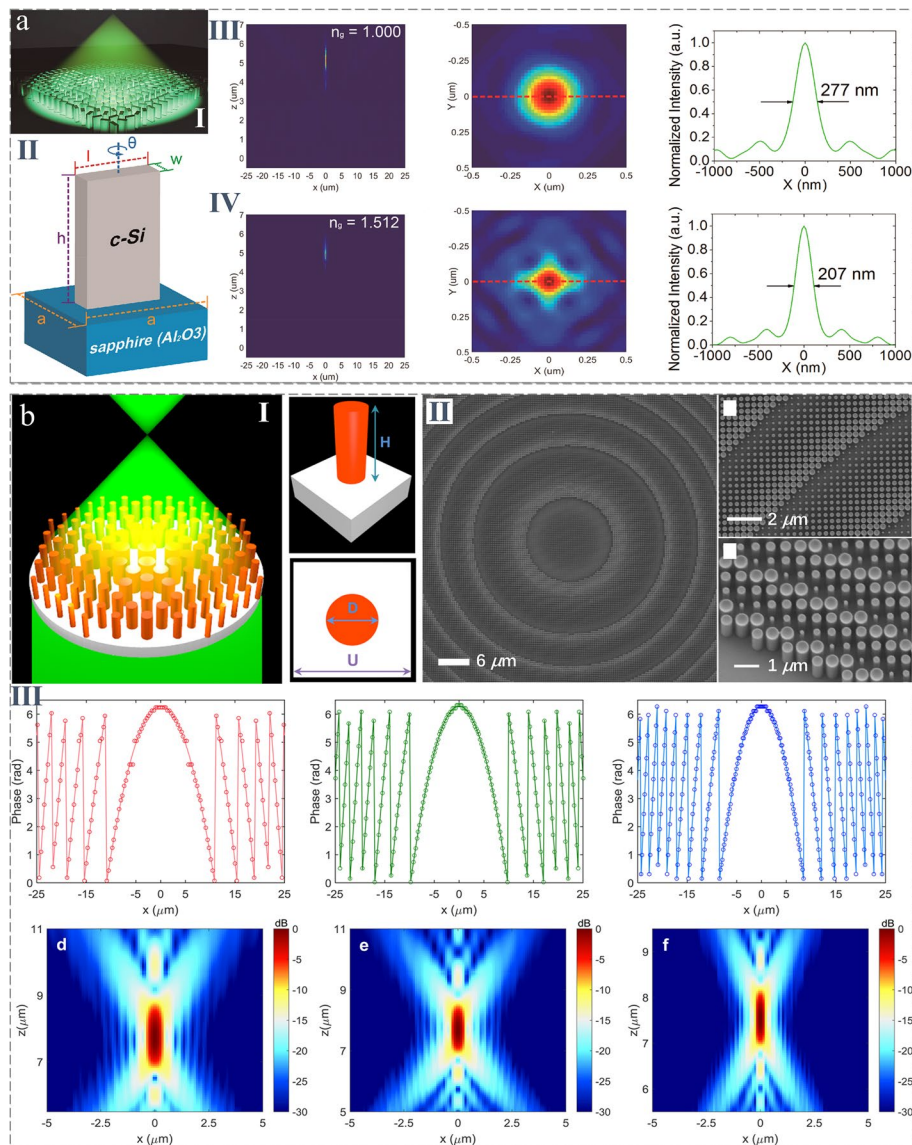


**Fig. 6** (a) (I) Schematic of the *c*-Si meta-lens. (II) Meta-lens consists of *c*-Si nanobricks on a sapphire substrate. Focusing performance of the meta-lens in air (III) and immersion oil (VI). (b) (I) Schematic of a meta-lens operating in transmission mode (left panel). Right panel: Side view and top view of the meta-lens building block. Top view SEM image of the center portion (left side of (II)) and a portion at higher magnification (right-top of (II)) of the fabricated meta-lens. Side view SEM image of the edge of the meta-lens (right-bottom of (II)). (III) Solid lines: required analog phase. Circles: digitized phase profiles of the meta-lenses designed at wavelengths of 660 nm (left), 532 nm (middle), and 405 nm (right). Corresponding 2D simulated intensity profiles at focal planes. (a) Reproduced with permission [160]. Copyright 2018, American Chemical Society (ACS). (b) Reproduced with permission [119]. Copyright 2016, ACS

Although the fabrication process was fully compatible with microelectronic technology and scalable, the optical loss of *c*-Si still increased as the frequency of the incident light increased, leading to the degradation of the performance in the visible regime. To overcome this problem, a new nanofabrication method called atomic layer deposition (ALD) [119] was utilized by Khorasaninejad et al. to develop a TiO<sub>2</sub> meta-lens (left side of Fig. 6b(I)) comprising waveguide-mode-like nanopillars that could control the

transmission phase based on the size of their diameters (right side of Fig. 6b(I)). Optical images of the sample are illustrated in Fig. 6b(II) for different scale bars. Three distinct meta-lenses with design wavelengths of 660 nm, 532 nm, and 405 nm were fabricated using EBL, and the phase profiles (first line of Fig. 6b(III)) were calculated using Eq. (1). These meta-lenses had the same diameter of 240 nm and an FL of 90 nm (second line of Fig. 6b(III)), yielding a NA of 0.8. In particular, owing to the high transparency of  $\text{TiO}_2$  in the visible spectrum and excellent accuracy, the highest focusing efficiency was 86% at an incident wavelength of 405 nm. However, the fabrication technique used for  $\text{TiO}_2$  metasurface relies on the ALD process, which is relatively slow and costly, and restricts the thickness and AR to less than 600 nm and 15, respectively [119, 152]. Currently, GaN meta-lenses are attracting much attention owing to their relatively well-developed and low-cost fabrication techniques that are used in the production of light-emitting diodes. Moreover, they can serve as a potential platform to study the interaction between nanostructures and a gain medium [196, 197]. Hence, Chen et al. demonstrated three individual GaN-based in-plane (Fig. 7a(I)) and off-axis (Fig. 7a(II)) meta-lenses that operated in a transmission window with extremely high operation efficiency for visible light (87% @ 633 nm; 91.6% @ 530 nm; 50.6% @ 430 nm) by utilizing the geometrical phase [164].

### UV wavelengths

Meta-lenses based on dielectric materials such as *c*-Si,  $\text{TiO}_2$ , GaN, etc. have recently been demonstrated to operate in the visible range with high focusing efficiency. However, they are hindered by the inter-band transitions of these materials (e.g., *c*-Si at  $\sim 1.1$  eV,  $\text{TiO}_2$  at  $\sim 3.2$  eV, and GaN at  $\sim 3.4$  eV), when operating in the UV band, and the corresponding device efficiencies are limited owing to significant absorption losses because of the relatively narrow bandgaps, which are low or near the minimum photon energy ( $\sim 3.26$  eV) of incident UV light. Therefore, the UV-transparent  $\text{Nb}_2\text{O}_5$  ( $\sim 3.65$  eV),  $\text{HfO}_2$  ( $\sim 5.7$  eV), and AlN ( $\sim 6.0$  eV) are appropriate choices for UV meta-lens design, both because of their wide bandgaps and high refractive indices [198].

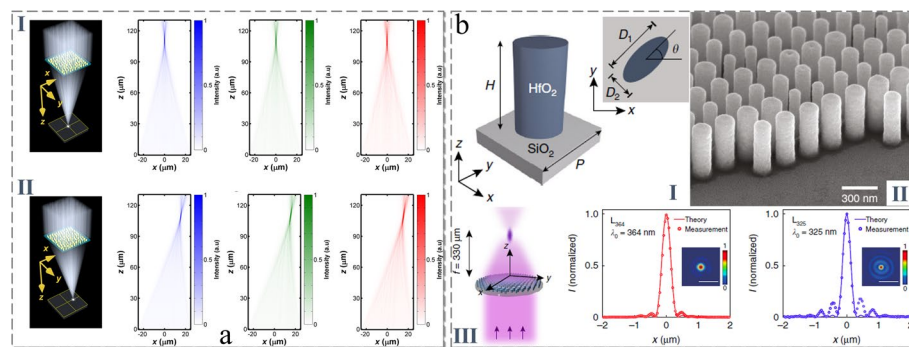


**Fig. 7** (a) Simulated focusing property from six distinct meta-lenses consisting of individual nanopillar arrays for red, green, and blue colors, respectively. Schematic of in-plane, on- (I) and off-axis (II) focusing meta-lens. Right side of (I) and (II): distribution of electric field intensity of the in-plane, on- and off-axis focusing meta-lens at the incident wavelengths of 430 nm (blue color map), 532 nm (green color map), and 633 nm (red color map). (b) (I) Schematic of a metasurface unit cell. (II) SEM image of the meta-lens. Left side of (III): Schematic of focusing. Right side of (III): Cross-focus cuts and intensity distributions in the focal plane. (a) Reproduced with permission [164]. Copyright 2017, ACS. (b) Reproduced with permission [142]. Copyright 2020, NPG

Zhang et al. demonstrated a high-NA (0.6) meta-lens that operated at UV wavelengths (364 nm and 325 nm), including wavelengths down to the DUV range [146]. The meta-lens was constructed using high AR  $\text{HfO}_2$  (which is UV-transparent and has a high refractive index) nanopillars on a quartz substrate (Fig. 7b(I)), which acted as a truncated dielectric waveguide with top and bottom interfaces of low reflectivity. This allowed for light propagation with a transmittance and phase shift controlled by the nanopillar height, nanopillar diameter, and lattice spacing. The optical image of the sample is shown in Fig. 7b(II). Two 500  $\mu\text{m}$  diameter, polarization-independent meta-lenses with identical NAs of 0.6 (corresponding to an FL of 330  $\mu\text{m}$  as shown in the left side of Fig. 7b(III)), were used to focus UV light at respective free-space wavelengths of 364 nm (middle side of Fig. 7b(III)) and 325 nm (right side of Fig. 7b(III)) and focusing efficiencies of  $55.17 \pm 2.56\%$  and  $56.28 \pm 1.37\%$ , respectively. The results of theoretical studies on UV meta-lenses have been reported based on  $\text{MgO}$  ( $\sim 7.8 \text{ eV}$ ),  $\text{Si}_3\text{N}_4$  ( $\sim 5.0 \text{ eV}$ ), and  $\text{AlN}$  nanoblocks [198], and based on careful pattern design, a calculated focusing efficiency as high as 94% (380 nm, the best value reported in the UV range so far) was achieved using a  $\text{MgO}$  meta-lens and the PB phase method [188]. Although this result has not been experimentally verified, the meta-lens exhibited great potential for promoting and improving the integration and miniaturization of UV photonic devices.

All the designs described in this section are based on Eq. (1), for which the nanoparticles are simulated at normal incidences using periodic boundary conditions. This design method assumes that the interaction between adjacent nanostructures in a meta-lens is similar to that in the periodic approximation without considering the actual near-field coupling among them. This directly results in perturbation of the wavefront and a reduction in the efficiency, even though the transmittance or reflection amplitude of the basic unit cell is highly optimized. This phenomenon is observed if the target phase profile changes slowly with the spatial coordinates (namely, the nanostructure geometry doesn't change too rapidly). In addition, this effect can be considered in the case of comprehensive full lens simulation followed by optimization to increase efficiency [199, 200].

### Operation bandwidth

Meta-lenses that operate at a dot frequency or narrow bandwidth can achieve high focusing efficiency, whereas, for the solar energy that reaches the surface of Earth, IR radiation makes up 49.4% while visible light accounts for 42.3%. UV radiation makes up over 8% of the total solar radiation as shown in Fig. 5(a) [18, 176, 177]. Hence, it is necessary to broaden the operation bandwidth of meta-lenses to match the solar spectra to achieve a better energy collection efficiency. In the case of a chromatic meta-lens, the FL changes as the incident wavelength is changed, resulting in a rainbow-like focal line when it is illuminated by a light source with a continuously changing wavelength (left side of Fig. 8(I)). Hence, achromatic meta-lenses (right side of Fig. 8(I)) with continuous operational wavelengths are in high demand for concentrating broadband planar light into one focal spot or line.

Initially, researchers attempted to eliminate chromatic aberration in a wide spectrum from  $\lambda_{\min}$  to  $\lambda_{\max}$  by directly introducing continuous phase compensation to Eq. (1), and therefore, it can be rewritten as [201]

$$\varphi(\rho, \lambda) = \varphi(\rho, \lambda_{\max}) + \Delta\varphi(\rho, \lambda) \quad (9)$$

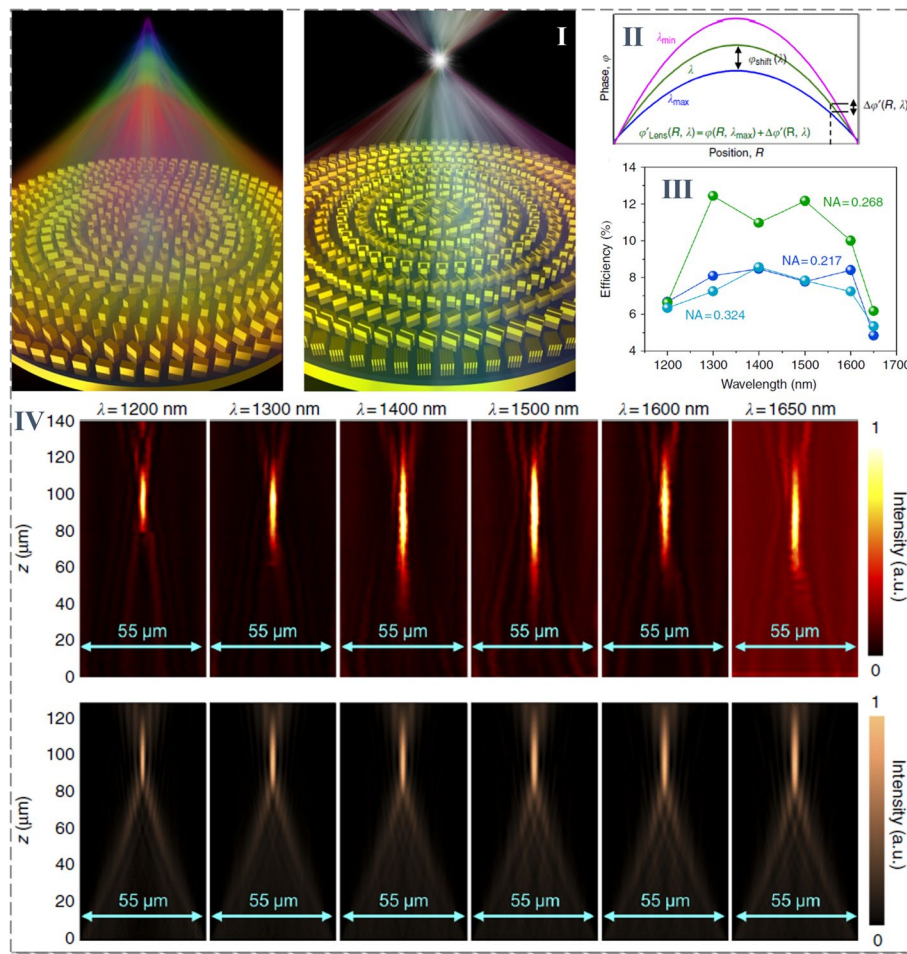


**Fig. 8** Schematic of chromatic (left side of (I)) and achromatic (right side of (I)) meta-lens. (II) Phase profile of a broadband achromatic meta-lens at an arbitrary wavelength. (III) Operation efficiency at the corresponding focal length as a function of wavelength. (IV) Experimental (top row) and numerical (bottom row) intensity profiles of broadband achromatic meta-lens along axial planes. Reproduced with permission [201]. Copyright 2018, NPG

where the former term on the right side of Eq. (9) denotes the essential phase profile at the wavelength  $\lambda_{\text{max}}$ . The required phase difference (latter term on the right side of Eq. (9)) varies with the incident wavelength and can be expressed as follows:

$$\Delta\varphi(\rho, \lambda) = - \left[ 2\pi \left( \sqrt{\rho^2 + f^2} - f \right) \right] \left( \frac{1}{\lambda} - \frac{1}{\lambda_{\text{max}}} \right) \quad (10)$$

which is a function of the operation wavelength (presenting a linear relationship with  $1/\lambda$ ) and requires elaborately designed resonators. Based on this approach, Wang et al. designed and experimentally validated a NIR meta-lens for removing chromatic aberration over a continuous wavelength region from 1200 nm to 1680 nm for circularly polarized incidence light in a reflection scheme [201]. By exploiting the geometric phase in combination with phase compensation from specially designed integrated-resonant unit elements (IRUEs, right side of Fig. 8(I)), the meta-lens could provide an exact phase profile (Fig. 8(II)) as the ideal requirement calculated using Eq. (10). It was capable of

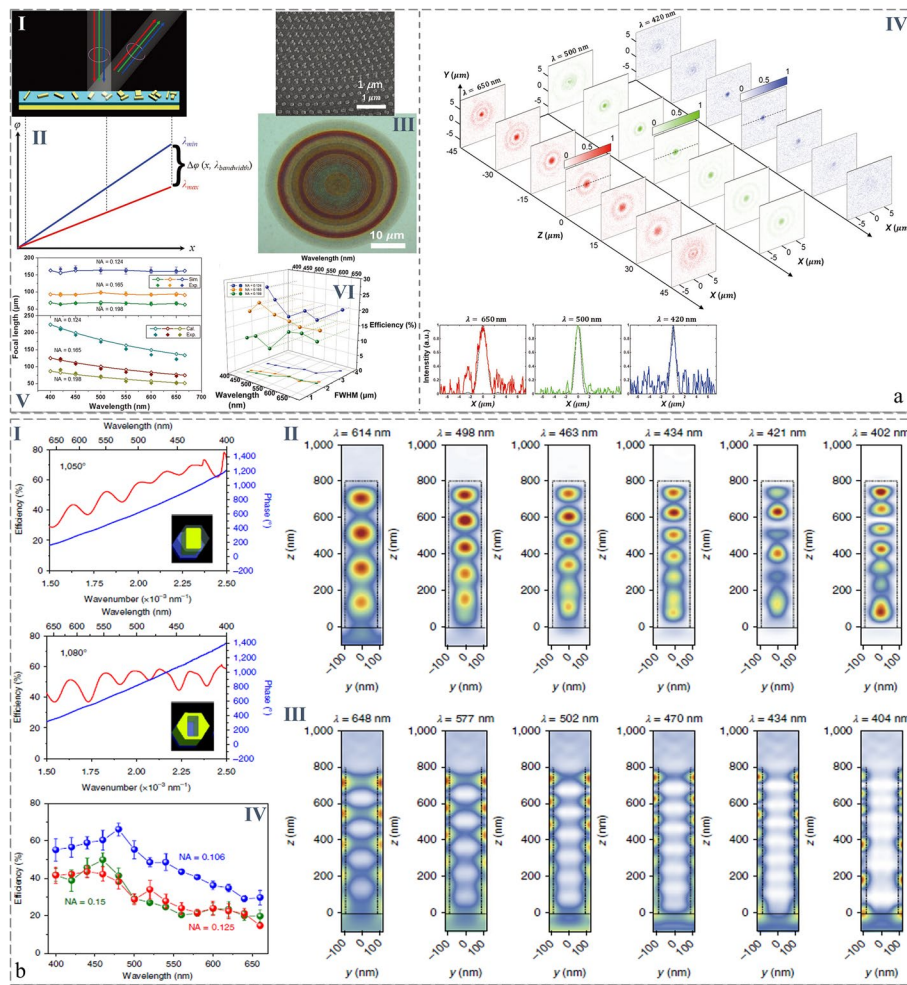


**Fig. 9** (a) Diagram of a broadband achromatic deflector (I) and its corresponding phase compensation profile (II). (III) Optical image (top) and SEM image (bottom) of fabricated meta-lens. (IV) Measured focused images at different focal planes. Insets show one-dimensional (1D) counterparts. (V) Simulated and measured FL as a function of wavelength for achromatic meta-lens (top) and chromatic meta-lens (bottom). (VI) Measured focusing efficiency (data points distributed in three-dimensional space) and FWHM (projection in the bottom plane) as a function of wavelength for three achromatic meta-lenses. (b) (I) Circularly polarized conversion efficiency (red curves) and phase profile (blue curve) of IRUEs with phase compensation of  $1050^\circ$  (top) and  $1080^\circ$  (bottom). Normalized magnetic energy for phase compensation of solid (II) and inverse nanostructures (III). (IV) Measured operation efficiency as a function of incident wavelength obtained for three achromatic meta-lenses. (a) Reproduced with permission [202]. Copyright 2017, NPG. (b) Reproduced with permission [165]. Copyright 2018, Wiley-VCH

focusing the plane waves within the operation wavelength at the same focal spot (first and second lines of Fig. 8(IV)). This represents the measured and numerical 2D mappings of focal spots, for which the average focusing efficiency was on the order of 12% (Fig. 8(III)). Subsequently, the analogous response phenomena have been successfully utilized for higher frequency light by selecting the appropriate building materials and adopting a similar method to fulfill the required phase compensation. Hsiao et al. proposed a special type of sandwich IRUEs with each building block (Al multi-nanorods/SiO<sub>2</sub>/Al) shown in Fig. 9a(I) comprised of one to a maximum of three nanorods depending on the required phase variation (Fig. 9a(II)). This was done to realize the smooth

and linear manipulation of the reflection-phase dispersion under circularly polarized illumination. By arranging these meta-atoms based on the phase profile calculated using Eq. (9) and (10), an achromatic meta-lens with various NA values was experimentally demonstrated. Fig. 9a(III) shows the optical image of the fabricated sample (top) and SEM image (bottom), which displayed an unvaried FL (Fig. 9a(IV) and top of Fig. 9a(V)) throughout the bandwidth of 420–650 nm compared to the chromatic meta-lens (bottom of Fig. 9a(V)) [202]. The focusing efficiencies of the achromatic meta-lens with an NA of 0.124 were 26.31%, 19.71%, and 20.37%, respectively, at wavelengths of 420 nm, 550 nm, and 650 nm (Fig. 9a(VI)). In addition, a broadband achromatic meta-lens operating in the visible region in transmission mode was demonstrated by Wang et al., and its basic meta-atoms composed of solid (top of Fig. 9b(I)) and inverse (bottom of Fig. 9b(I)) nanostructures were designed and fabricated by utilizing low-loss semiconductor GaN to access waveguide-like modes (Fig. 9b(II–III)) in the visible spectrum (from 400 nm to 660 nm) [165]. Using similar integrated resonances, the required retarding phases (Fig. 9b(I)) were obtained to converge the broadband planar light with an identical FL, NA of 0.106, and an average efficiency of approximately 40% (Fig. 9b(IV)).

In the following, to further optimize the strategy for guiding the design of achromatic meta-lenses operating at continuous wavelengths, Chen et al. expanded Eq. (1) around the target angular frequency  $\omega_0$  using a Taylor series expansion as follows [152]:

$$\varphi(\rho, \omega) = \varphi(\rho, \omega_0) + \left. \frac{\partial \varphi(\rho, \omega)}{\partial \omega} \right|_{\omega=\omega_0} (\omega - \omega_0) + \left. \frac{\partial^2 \varphi(\rho, \omega)}{\partial \omega^2} \right|_{\omega=\omega_0} (\omega - \omega_0)^2 + \dots \quad (11)$$

The first term (namely the basic phase profile at  $\omega_0$ ) on the right side of Eq. (11) leads to a spherical wavefront, and the group delay term  $\partial \varphi(\rho, \omega) / \partial \omega$  compensates for the different arrival times of wavepackets at the focus. The group delay dispersion  $\partial^2 \varphi(\rho, \omega) / \partial \omega^2$  ensures that the outgoing wavepackets are identical. Eq. (11) can be expressed as the principal diagram shown in Fig. 10a(I), and the meta-lens is designed to provide spatially dependent group delays such that wavepackets from different locations arrive simultaneously at the focus. The yellow line shows the spherical wavefront. The net effect is the minimization of the spread in the arrival times of the wavepackets at the focus to ensure they constructively interfere. The smaller the time spread, the larger the bandwidth achieved. Therefore, to realize diffraction-limited focusing for a wide bandwidth, both phase and group delay, as well as higher-order terms, need to be appropriately controlled.  $\varphi(\rho, \omega_0)$  can be commonly tuned using PB phase modulation or the propagation phase method, whereas the other two terms can be adjusted by optimizing the waveguide modes relative to the effective refractive and structural parameters of the meta-atoms. Based on the aforementioned design method, they first proposed a broadband achromatic meta-lens for focusing incident visible light. The meta-elements consisted of one or more  $\text{TiO}_2$  nanofins of varying dimensions, but equal height and period (left side of Fig. 10a(II)), for which the required transmittance phase and dispersion could be independently imparted using the geometric phase and waveguide mode. Based on the simple single-layer design (SEM image on the right side of Fig. 10a(II)), a meta-lens with an NA of 0.2 and focusing efficiency of approximately 20% was achieved for wavelengths ranging from



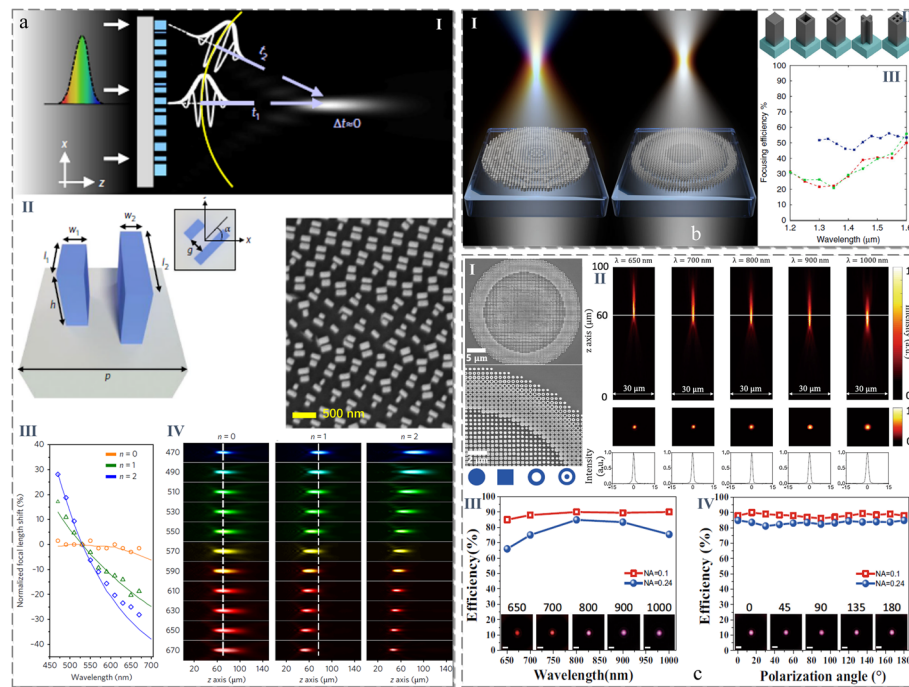


**Fig. 10** (a) Dispersion engineering of meta-lens: (I) Principal diagram of an achromatic meta-lens; (II) Schematic of a meta-lens element and SEM of a region of a fabricated meta-lens; (III) Measured normalized FL shifts (symbols) compared to simulations (lines) for meta-lens; (IV) Measured intensity distributions in the focal plane. (b) Schematic of a monochromatic meta-lens (left side of (I)) and a broadband achromatic meta-lens (right side of (I)). (II) Schematic of meta-unit archetypes. (III) Measured focusing efficiencies of the meta-lenses. (c) (I) Top view SEM images of achromatic meta-lens with four types of nanostructures. 2D (top panels of (II)) and 1D (bottom panels of (II)) intensity profiles of focal spots in focal planes. (III) Experimentally recorded focusing efficiency of the  $\text{TiO}_2$  meta-lens. (IV) Dependence of the focusing efficiencies on the polarization at 800 nm. (a, b) Reproduced with permission [152, 169]. Copyright 2018, NPG. (c) Reproduced with permission [203]. Copyright 2021, NPG

470 nm to 670 nm (Fig. 10a(III-IV)). In the same year, Shrestha et al. introduced a transmission-type achromatic dielectric meta-lens that crossed a wide NIR bandwidth for any arbitrary polarization states (right side of Fig. 10b(I)) [169]. The proposed *a*-Si patterns had four-fold symmetry instead of rotational symmetry and achieved more geometric degrees, leading to large phase differences (Fig. 10b(II)). The aperture profile was then transferred to the *a*-Si film using inductively coupled plasma (ICP) etching, and the focusing efficiency of the fabricated meta-lens increased by 50% across a continuous and wide bandwidth from 1200 nm to 1650 nm (Fig. 10b(III)). Afterward, to address the limitation that corrected chromatic aberration suffers from markedly reduced focusing efficiency, Balli et al. presented a hybrid achromatic GaN meta-lens that could improve focusing efficiency over a broad wavelength range from 1000 nm to 1800 nm [178]. The optimized meta-atoms were designed by combining recursive ray tracing and simulated phase libraries, instead of computationally intensive global search algorithms to realize a higher conversion efficiency and desired phase dispersion. They experimentally verified that the meta-lens with an NA of 0.66 had an average focusing efficiency greater than 60%.

To simultaneously cover the partially visible light and NIR spectra, Ndao et al. proposed a polarization-independent fishnet-achromatic meta-lens to address the

intrinsic dispersion of the existing materials, and its average efficiency exceeded 70% in the continuous band from 640 nm to 1200 nm. This enables applications that require broad bandwidth and high efficiency, including solar energy harvesting [204]. The building blocks made of  $\text{TiO}_2$  were regarded as cross-circle waveguides that could flexibly control the slope and the intercept of the phase shift, and were suitable for eliminating wideband chromatic aberration. Recently, to maximize the focusing efficiency while not affecting the operational bandwidth, Wang et al. experimentally demonstrated a polarization-insensitive, broadband  $\text{TiO}_2$  achromatic meta-lens (SEM images in Fig. 10c(I): top for the top view of the entire structure; bottom for the partially enlarged view) for applications in NIR biological imaging [203]. A large-scale fabrication technology was developed to produce  $\text{TiO}_2$  nanopillars with record-high ARs ( $\sim 37.5$ ) featuring pillar heights of 1.5  $\mu\text{m}$  and nearly 90 degrees vertical sidewalls. The demonstrated meta-lens exhibited a dramatically increased group delay range, and the spectral range of achromatism (Fig. 10c(II)) was substantially extended to the wavelength range of 650–1000 nm with an average efficiency of 77.1%–88.5% and a numerical aperture of 0.24–0.1 (Fig. 10c(III)). In addition, owing to the symmetrical features, the proposed meta-lens can operate at a high level without considering the polarization states (Fig. 10c(IV)).

Even though ultra-broadband meta-lenses that operate from the visible region to the NIR spectrum have been successfully developed with improved focusing efficiency, there is still a lack of experimental research on broadband UV meta-lenses in relation to processing capability constraints. To date, only a few theoretical studies have been conducted on broadband achromatic UV meta-lenses [188, 190–192]. For example, Kanwal et al. [188, 190] and Liu et al. [192] theoretically investigated two types of UV meta-lenses that could react with broadband UV light of 270–380 nm and 300–400 nm. These two polarization-independent meta-lenses were composed of cylindrical  $\text{Si}_3\text{N}_4$  or AlN nanopillars, respectively, with focusing efficiencies of approximately 40% and 50%.

In conclusion, achromatic focusing essentially requires the different wavelengths to obtain the same group delay by optimizing the dispersion of the nanostructure. However, the group delay determining the working bandwidth is limited because it is fundamentally governed by the height of the nanostructure divided by its group index. The trade-off between the NA, diameter, and group delay of broadband achromatic meta-lenses [152, 169, 205] proves that further increasing the height of the nanostructures can improve the group delay, but result in an increased AR, thereby causing fabrication challenges (Table 1).

### Angular stability

In addition to achieving high-efficiency broadband achromatic meta-lenses, from Fig. 11(a), simultaneously considering that the Earth's rotation and revolution have a significant influence on the incident angle of sunlight, maintaining the focused light on one spot, along one line, or across one plane when the incident angle varies is an important issue. Several attempts have been made to address this problem to improve the field of view (FOV) and eliminate the off-axis aberrations of meta-lenses [209–214]. Generally, once the aperture phase of a metasurface is in accordance with [100]

**Table 1** Performance metrics of the meta-lenses presented in this paper

Mat. <sup>a)</sup>	Type/Pol. <sup>b)</sup>	W.L. <sup>c)</sup> (nm)	Eff. (% <sup>d)</sup> )		N.A.	F.L. ( $\mu$ m)	Diam. <sup>e)</sup> ( $\mu$ m)	A.R. (Max.)	F.O.V. (Deg.)	Ref. f)
			Mean	Peak						
Al	R/CP	420–650	–	26.31@420nm	0.124	163	41.86	–	–	[202]
Au	R/CP	1200–1680	~12	12.44@1300nm	0.268	100	55.55	–	–	[201]
Au	T/CP	1500–1630	–	16.4@1540nm	0.23	40–41.3	~25	–	–	[112]
Au	T/CP	676	–	~10	0.62	2.5	4	–	–	[98]
Al/Ag/Au	T/CP	450,550,650	–	5.8–8.7	–	1000	–	–	–	[206]
HfO <sub>2</sub>	T/CP	325	–	56.28 ± 1.37	0.6	330	500	~7.1	–	[146]
AlN	T/CP	376	–	47.1	–	662	4 × 4	12	–	[148]
Si <sub>3</sub> N <sub>4</sub>	T/CP	250–400	–	77@400nm	~0.75	2.9–5.3	10	~2.5	–	[188]
MgO	T/CP	182	–	94	~0.8	7.56	20	12	–	[189]
GaN	T/LPCP	1000–1800	61	83@1800nm	0.27	34.5	20	~7.3	–	[178]
$\alpha$ -Si	T/LPCP	1550	–	~82	–	500	400	4.7	–	[175]
c-Si	T/LP	640	–	~67	0.8	0.34	64	–	–	[195]
TiO <sub>2</sub>	T/LPCP	405,532,660	–	30,70,90	0.6	200	300	7.5	–	[141]
GaN	T/CP	430,530,633	–	87,91,650.6	0.164	300	100	~3.3	–	[164]
GaN	T/CP	400–660	40	67@475nm	0.106	235	–	16	–	[165]
TiO <sub>2</sub>	T/CP	470–670	–	~37@500nm	0.02	–	160	12	–	[152]
$\alpha$ -Si	T/LPCP	1200–1650	~50	–	0.24	200	100	–	–	[169]
TiO <sub>2</sub>	T/LPCP	640–1200	~70	75@800nm	0.12	~40	10	–	–	[204]
TiO <sub>2</sub>	T/LPCP	650–1000	~88.5	90.2@700nm	0.1	~110	25	~37.5	–	[203]
$\alpha$ -Si	/LP	1100–1700	~50	–	–	74.5	190 × 100	17.5	120	[100]
PbTe	T/LP	5200	–	32–45	0.24	2000	5200 × 5200	1.25	~170	[174]
$\alpha$ -Si	T/LPCP	940	–	41–88	0.2	2500	6400 × 6400	7.5	~180	[174]
$\alpha$ -Si	T/LP	850	–	45–70	0.49	717	800	–	60	[207]
TiO <sub>2</sub>	T/CP	532	–	~50	0.44	342.5	–	~6.3	50	[153]
$\alpha$ -Si	T/LPCP	740	–	–5	0.71	203	500	3.5	160	[208]

<sup>a</sup> Mat. Material. <sup>b</sup> Pol. Polarization, <sup>c</sup> W.L. Wavelength. <sup>d</sup> W.L. Wavelength. <sup>e</sup> Diam. diameter, <sup>f</sup> Ref. Reference.

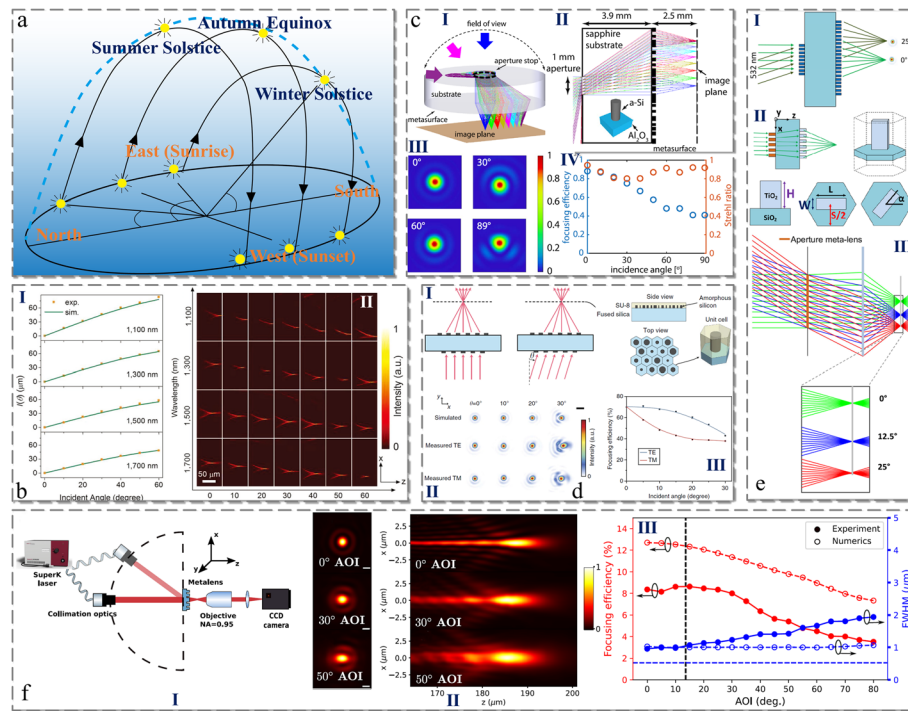


**Fig. 11** (a) Schematic of the sun's annual trajectory over Wuhan. (b) Experimental demonstration of the Fourier meta-lens with oblique incidence. (I) Measured and simulated foci offset with different incident wavelengths and angles. (II) Intensity distribution of the focal images for different incident angles and wavelengths. (c) Schematic (I) and side view (II) of a single-layer planar meta-lens with an ultrawide FOV. Inset: meta-atom configuration. Simulated focal spots (III), Strehl ratio, and focusing efficiency (IV) at different angles of incidence. (d) Schematic of focusing on- and off-axis light by a metasurface doublet lens (left side of (I)) comprised of dielectric meta-atoms (right side of (I)). Simulated (top row of (II)) focal intensity profiles, measured (middle and bottom row of (II)) for TE and TM mode) and measured focusing efficiency (III) of the metasurface doublet lens for different incident angles. (e) A schematic of the meta-lens doublet (I) comprising two meta-lenses: aperture meta-lens (depicted in orange of (II)) and focusing meta-lens (depicted in light blue of (II)), where each meta-lens consists of an array of rotated nanofins (bottom line of (II)). (III) Ray diagram for diffraction-limited focusing along the focal plane. Inset: magnified plots near their focal planes. (f) (I) Schematic of the optical setup for characterization. Normalized point spread function images and intensity distributions (second column of (II)) measured in the focal plane for angles of incidence of  $0^\circ$ ,  $30^\circ$ , and  $50^\circ$ . (III) Focusing efficiency and FWHM of the point spread function as a function of the angle of incidence. (b) Reproduced with permission [100]. Copyright 2018, Wiley-VCH. (c) Reproduced with permission [174]. Copyright 2020, ACS. (d) Reproduced with permission [207]. Copyright 2016, NPG. (e) Reproduced with permission [153]. Copyright 2017, ACS. (f) Reproduced with permission [208]. Copyright 2021, ACS

$$\Phi(\rho, \theta) = \gamma \sin \theta + \sqrt{1 + \left(\gamma - \frac{l(\theta)}{f}\right)^2} - \sqrt{1 + \left(\gamma + \frac{l(\theta)}{f}\right)^2} \quad (12)$$

where  $\Phi(\rho, \theta) = -\phi/k_0 f$  and  $\gamma = \rho/f$  are the normalized phase and radius, perfect meta-lenses can be constructed that show good performance for large incident angles and broad bandwidth. Eq. (12) illustrates that each incident angle  $\theta$  that corresponds to a focus in the focal plane should be accompanied by a focal offset of  $l(\theta)$  from the origin. To achieve the desired focusing functionality based on Eq. (12), an abrupt phase retardance  $\phi$  is required along the surface of the meta-lens to compensate for the phase accumulated via propagation. By applying Eq. (12) and the waveguide modes introduced by  $\alpha$ -Si microstructures, a single-layered Fourier meta-lens with a large NA and negligible

angular dispersion at large incident angles was realized by Liu et al., which showed good performance for incidence angles in the range of 0–60° covering a broad bandwidth from 1100 nm to 1700 nm (Fig. 11b(I)) and a focusing efficiency of more than 30%. However, the FLs are different owing to frequency dispersion (Fig. 11b(II)) [100]. To further extend the FOV, the angle stability is optimized at larger incident angles. Shalaginov et al. presented results for a novel Huygens meta-lens (Fig. 11c(I-II)) capable of diffraction-limited focusing on identical focal planes over an angular FOV of approximately 180° (Fig. 11c(III)). The corresponding focusing efficiency at the wavelength of 940 nm fluctuated from 41% to 88% owing to the variation of the incident angles (Fig. 11c(IV)) [174]. In this work, *a*-Si nanoposts (inset of Fig. 11c(II)) with a uniform height of 750 nm, diameter ranging from 100 nm to 250 nm, and a fixed lattice constant of 450 nm, were designed and modeled utilizing a hierarchical combination of full-wave and Kirchhoff diffraction integrals to acquire the appropriate angular dispersion.

Another method that is analogous to the traditional cascaded multiple lenses was proposed to treat the monochromatic aberrations generated owing to the influence of oblique incident light by utilizing the double-layered meta-lenses, which has the additional benefits associated with miniaturizing the optical elements. For example, Arbabi et al. proposed a doublet *a*-Si meta-lens by cascading two metasurfaces linked with fused-SiO<sub>2</sub> substrate to correct the on- (left side of Fig. 11d(I)) and off-axis (middle side of Fig. 11d(I)) aberration [207]. The phase profiles were defined as even order profiles polynomials of the radial coordinate  $\rho$  as follows:

$$\varphi(\rho) = \sum_{n=1}^5 a_n \left(\frac{\rho}{D}\right)^{2n} \quad (13)$$

where  $D$  is the radius of the meta-lens and  $\rho$  is the radial coordinate. The coefficients  $a_n$  were optimized to minimize the focal spot size (root mean square spot size) at incident angles up to 30°. The phase profiles of the two metasurfaces composing the doublet lens were obtained via a ray tracing technique, and the design could focus oblique planar incident light (from –30° to 30°, Fig. 11d(II)) at a wavelength of 850 nm onto the same plane to achieve a focusing efficiency of more than 40% for both TE and TM waves (Fig. 11d(III)). These two linked metasurfaces were constructed using an array of *a*-Si nanoposts covered with a layer of SU-8 polymer (right side of Fig. 11d(I)) to continuously control the transmission phase-shifting process by utilizing waveguide modes and arranging them in a hexagonal lattice. Using this design scheme, Groever et al. demonstrated a compact meta-lens doublet by patterning two TiO<sub>2</sub> metasurfaces on both sides of a SiO<sub>2</sub> substrate (Fig. 11e(I)) [153]. One of these metasurfaces acted as an aperture meta-lens (the phase profile was calculated using Eq. (13), and is depicted in orange in Fig. 11e(II)) to correct for spherical aberrations and to realize diffraction-limited focusing along a focal plane. The other was a focusing meta-lens which facilitated the correcting of aberrations (depicted in light blue in Fig. 11e(II)). The phase of the focusing meta-lens was chosen as

$$\varphi(\rho) = -\frac{2\pi}{\lambda_0} \left( \sqrt{\rho^2 + f^2} - f \right) + \sum_{n=1}^5 b_n \left(\frac{\rho}{D}\right)^{2n} \quad (14)$$

This design had a NA of 0.44, an FL of 342.5  $\mu\text{m}$ , and a FOV of 50° that enabled diffraction-limited monochromatic focusing along the identical focal plane, and the focusing efficiency fluctuated from 30% to 50% as the incident angle increased from 0° to 25° (Fig. 11e(III)). Since the basic nanofins (Fig. 11e(II)) were modulated using the BP phase strategy, this meta-lens could only interact with the circularly polarized incident light.

Recently, quadratic phase profiles have been widely adopted for wide FOV meta-lens design due to the higher tolerance of the focusing efficiency at oblique incidences compared to hyperbolic lenses [208, 215–218]. For example, Lassalle et al. demonstrated a quadratic meta-lens for fingerprint detection [208]. To design this meta-lens, *a*-Si nanopillars with different diameters were chosen to map the  $2\pi$ -wrapped phase profile given as

$$\varphi(\rho) = \varphi(0) - \frac{2\pi n_t}{\lambda_0} \frac{\rho^2}{2f} \quad (15)$$

where  $n_t$  is the refractive index of the medium that the light traverses. As the incident angle increased from 0° to 80°, the fabricated meta-lens with an NA of 0.71 could focus the incoming light at a wavelength of 740 nm along a line parallel to the aperture. By exploiting the optical setup shown in Fig. 8f(I), normalized point spread function images (first column of Fig. 11f(II)) and intensity distributions (second column of Fig. 11f(II)) were measured for 0°, 30°, and 50° angle of incidences, which resulted in focal spots with almost identical FLs. However, owing to the intrinsic consequence of the combination of spherical aberration and the effective NA of the quadratic lens, this design only exhibited a focusing efficiency of approximately 10% when exposed to orthogonal polarization fields (Fig. 11f(III)). Similar phenomena could be observed in related works [215–218].

In this section, the equations (Eq. (11–14)) are carefully examined that link the inherent trade-off between the diameter, the FL, and the phase profile of meta-lenses with angular stability. The angular dispersion of a single meta-lens can be designed by globally optimizing the phase function of the building blocks according to Eq. (12) and (15) or using a corrector to form a doublet meta-lens based on Eq. (13, 14). However, given that the phase imparted by each nanostructure depends on the angle, the efficiency of a meta-lens varies with the angle of incidence. In principle, the larger the incident angle, the lower the focusing efficiency (Fig. 11). Therefore, it is still challenging to maintain the robust and high efficiency of a meta-lens over a large angular range. To address this challenge, more innovative strategies are needed to construct the wide angular dispersion of a meta-lens.

### Fabrication method

We have established the functional features of a meta-lens that is used for solar energy harvesting, as well as the corresponding design methods to achieve the required performance. In the following, the large-area manufacturing technologies of the meta-lens will be carefully introduced to realize a closed-loop from theoretical design to practical application.

The large-area fabrication process is the last and deciding step as the flat meta-lens transition from lab to fab. Unlike the miniaturized imaging devices that are used for holographic imaging, augmented reality, VR, detectors, sensors, cameras, etc., solar

collectors have large profiles and sizes to gather more light energy. However, although the traditional semiconductor fabrication methods such as EBL and focused ion beam (FIB) milling exhibit very high machining precision, their time consumption, and extremely high cost are untenable for the preparation of large-scale nanodevices for marco applications. In addition, considering their relatively low final pass yield in large-area processing, the stepper processing technology is now mainstream for realizing large-area functional devices based on the superposition of small pieces [181, 206, 219–221]. For example, a 2 cm diameter *a*-Si (deposited by plasma-enhanced chemical vapor deposition) meta-lens operating at 1550 was patterned using a stepper (GCA AS200 i-line 365 nm stepper, as shown in Fig. 12a(I), and the corresponding 600 nm tall nanopillars (Fig. 12a(II)) were etched using RIE [206]. The focusing efficiency of the obtained meta-lens can reach  $91.8 \pm 4.1\%$  at the predesigned frequency (Fig. 12a(III)). Due to the utilization of the photolithographic stepper, repeated exposure combined with a precise displacement system can be implemented to pattern a large number of identical meta-lenses with a fixed edge-to-edge gap on a 4-in. glass substrate as shown in Fig. 12a(I). Using the same processing strategy, Park et al. prepared a centimeter-scale, all-glass meta-lens that was capable of focusing and imaging at visible wavelengths, using an elaborate selective etching process to improve the thickness and AR of the pattern layer [219]. During the fabrication procedure, as illustrated in Fig. 12b(I), the deposited chrome (Cr) film was dry-etched (ICP-RIE) on a 100 mm diameter SiO<sub>2</sub> wafer using a DUV lithography patterned resist as the etching mask and utilizing chlorine (Cl<sub>2</sub>). SiO<sub>2</sub> was thermodynamically protected against chemical etching using Cl<sub>2</sub> plasma. Therefore, Cl<sub>2</sub> provided high etch selectivity for Cr over SiO<sub>2</sub>. The SiO<sub>2</sub> wafer was then dry-etched (ICP-RIE) until the etch depth reached 2 μm using Cr as the hard etch mask with trifluoromethane/argon (CHF<sub>3</sub>/Ar) gas. CHF<sub>3</sub> had a slow Cr chemical etch speed compared to that of SiO<sub>2</sub>, so Cr was suitable as an etch mask. Finally, the remaining Cr was removed using ICP-RIE with the Cl<sub>2</sub> plasma leaving only SiO<sub>2</sub> nanostructures. Fig. 12b(II) and 12b(III) show the tilted and top view SEM images of the patterned nanopillars of the obtained meta-lens. In combination with a DUV projection stepper lithography and a source wavelength of 248 nm, 45 1 cm diameter meta-lenses were obtained with a focusing efficiency of 45.6% at 633 nm on a 4-in. fused-SiO<sub>2</sub> wafer (Fig. 12b(IV)), showing the size-scalability and potential for mass-production.

More inspiring, 12-in. flat optics platforms (the maximum size recorded) for polarization conversion, beam bending, color display, and focusing have been achieved by using an immersion scanner which has the same function as the stepper, but has better resolution owing to the liquid medium padding (between the lens and wafer) with a refractive index greater than one [222–225]. Using this approach, Hu et al. investigated a group of *a*-Si meta-lenses operating at 940 nm and fabricated on a 12-in. glass wafer for fingerprint imaging (Fig. 13(I)) [225]. The 193 nm ArF DUV immersion lithography process was used to pattern their design with critical dimensions as small as 100 nm. Panels (II) and (III) of Fig. 13 show the top view SEM images of the central and near-central zones of the meta-lens, respectively. Fig. 13(IV) shows a zoomed-in angled view SEM image of the pillars close to the edge of the meta-lens. The diameters of these nanopillars changed from large to small values to cover the phase shift from 0 to  $2\pi$ . The measured results (Fig. 13(V–VII)) show the fabricated meta-lens had a measured focusing efficiency of

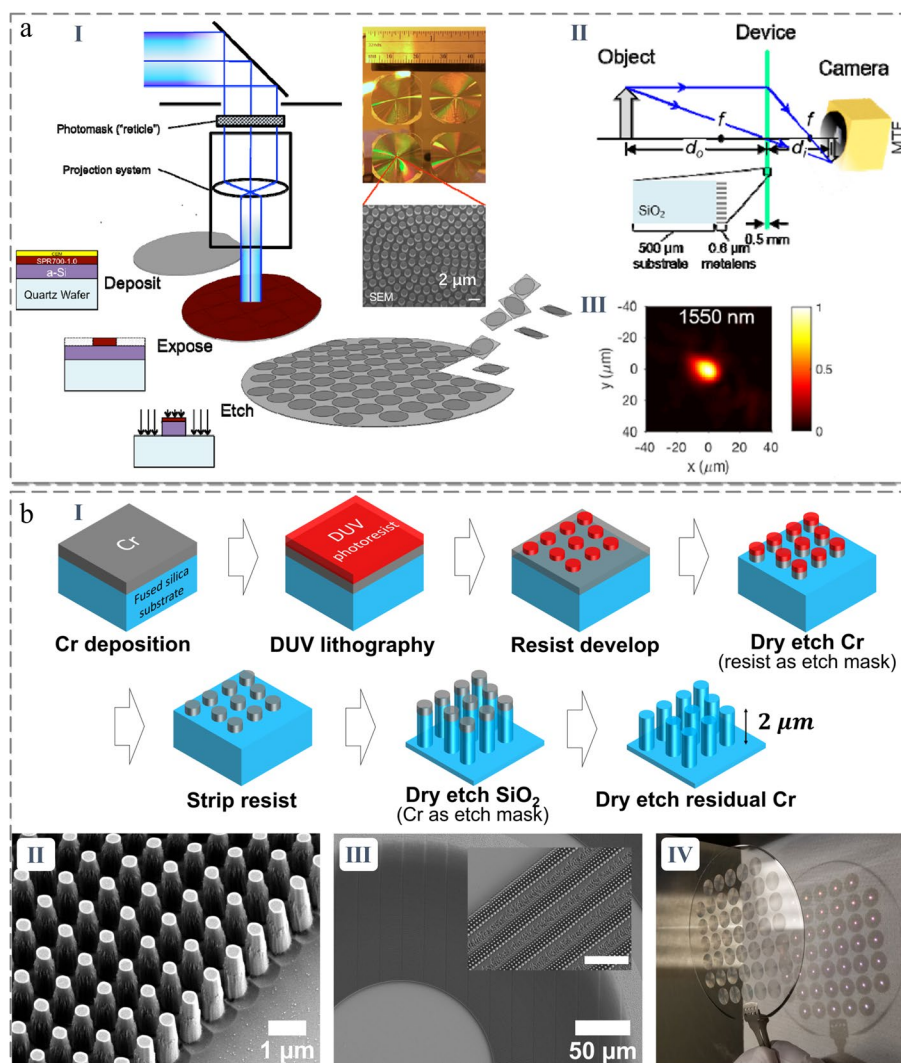


**Fig. 12** (a) (I) Schematic showing the production of meta-lenses at low cost and high yield using existing photolithographic stepper technology. The pattern of the meta-lens contained in the reticle was then projected into the stepper, and rapidly replicated over the face of the wafer by repeatedly exposing and incrementally stepping the wafer position. An SEM of the meta-lens center (center right) shows the microscopic posts. (II) The fabricated meta-lens for imaging. (III) Image of focal spot with 7 mm Gaussian illumination at 1550 nm. (b) (I) Fabrication process of the designed meta-lens using the selective etching process. (II) Zoom-in SEM image (tiled) of nanopillars of the meta-lens with a sidewall angle of 2.85°. (III) Top view SEM image near the center, and the inset shows the image of the edge of the lens. (IV) Image of 45 fabricated 1 cm meta-lenses on a 4-in.-diameter SiO<sub>2</sub> wafer, focusing incident light on a white sheet of paper. (a) Reproduced with permission [206]. Copyright 2018, OSA. (b) Reproduced with permission [219]. Copyright 2019, ACS

29.2%, an FL of 1.73 mm, and a FWHM of 1.26, overlaying an ideal Airy function with an aperture of 2 mm and a focal length of 1.75 mm. The immersion lithography accompanied by the dedicated etching process developed in this work can be used to fabricate meta-lenses that operate at even shorter wavelengths, i.e., the visible regime, thereby providing a promising solution for the mass manufacturing of metasurface-based solar energy concentrators. However, once the aforementioned methods are employed, the EBL or FIB with low processing efficiency is first needed to fabricate the mask, the size



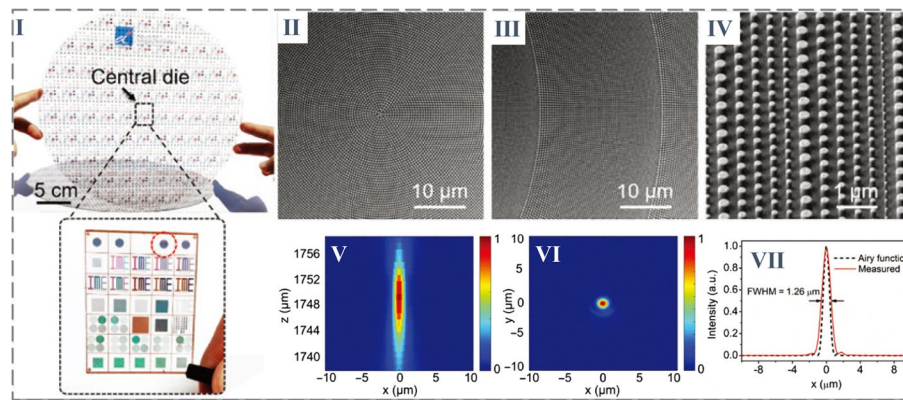


**Fig. 13** Characterization of the meta-lens fabricated on a 12-in. glass wafer: (I) Color images of the fabricated 12-in. glass wafer and the central die in the wafer, with highlighted areas indicating the meta-lens. SEM images were obtained at the central (II), near-central (III), and outer zones (IV) of the meta-lens. Measured optical intensity of the meta-lens at the optical propagation plane (V) and the focal plane (VI). (VII) Horizontal cut of the focal spot is shown in (VI). Reproduced with permission [225]. Copyright 2020, published by De Gruyter

of which determines the final area of the obtained meta-lens for the following lithography. The one-time exposure area of the steppers or scanners is limited and confines the size of the fabricated meta-lens. Therefore, the maximum diameter of a complete meta-lens can only reach the order of centimeters, far from that of a sunlight collector. In addition, current manufacturing processing is not ideally suited for whole-plane nanofabrication (with a tiny gap between the pattern arrays) on a large-area wafer, and only discrete meta-lenses with identical functionality can be fabricated as shown in Fig. 12a(I), 12b(IV) and 13(I). It is also challenging to manufacture meta-lenses in the visible range (particularly at shorter wavelengths) with high efficiency due to the resolution limitations.

## Conclusions and outlook

In summary, we have reviewed the research motivation, design principles, building materials, and large-area manufacturing strategy of meta-lenses for solar energy harvesting in terms of focusing efficiency, operation bandwidth, and angular stability. Evidently, the innovations in fundamental design strategies, advanced materials and manufacturing techniques of meta-lenses have paved a promising path in the field of solar-thermal collection and other photonic applications. Some of metasurface theory and related technologies are not examined here due to their low relevance to the energy field, though they have resulted in numerous novel features that have already been attached to the original platform, such as reconfigurability [226–233], artificial intelligence [234, 235], nonlinearity [139, 236–241], etc.

Encouragingly, various approaches for enhancing focusing efficiency, broadening the operating bandwidth, and improving the incident angular stability have been proposed to promote the efficient use of solar energy, resulting in encouraging signs. However, unlike traditional refractive lenses, it is difficult for meta-lenses to capture all the transmitted or reflected light. Instead, there is usually uncoupled incident light that scatters anomalously without desired phase delays, resulting in background noise and secondary foci. These

phenomena directly lead to the degradation of the focusing efficiency. In addition to the focusing performance, meta-lenses so far developed show inferior environmental adaptability and mechanical stability to the traditional mirrors. This is because they consist of numerous building blocks mainly at the nanoscale (1 nm–100 nm) or the order of the sub-micron (100 nm–1  $\mu$ m). These nano-structures are easy to be irreversibly damaged when the large-sized concentrator is applied with external force. Their basic materials may suffer from remarkably decreased chemical stability as a result of the large specific surface area, directly affecting its service life. Furthermore, meta-lenses are vulnerable to be polluted by the ambient dust et al., owing to their ultra-small-sized components, but actually the maintenance of the meta-lens is much more difficult than that of the standard mirror. Of course, if the meta-lens can be protected with an environmental isolation layer or embedded in a substrate with a low refractive index and loss, the frangibility mentioned above will be significantly improved. In principle, the planar meta-lens used for solar energy concentration is hardly superior to their classical counterparts without phase dispersion, but there is still room for improvement in terms of meta-lens-based solar-thermal application as follows:

- I Regarding the solar energy collectors as shown in Fig. 1(b), the absorbers (located at the light focal places) aiming to convert solar energy to thermal flux for further manipulation, have an enormously larger size compared to that of the sunlight wavelengths, i.e., strict achromatism is not necessary, and the system needs to confine the solar light with an effective heating effect into a relatively large zone (equal to the maximum cross-section of the absorbers) not a spot desiring for high resolution. In the concerned region, the distribution form of the dispersive light (even a rainbow-like distribution) makes little difference to the performance of the solar-thermal system. Therefore, the design principle of the metasurface-based concentrators can be relaxed according to the actual size of the absorbers, thereby facilitating the utilization of the ultra-broadband sunlight. Additionally, the range of group delay can be increased by cascading nanostructured multilayers for achromatic and wide FOV meta-lens design, but great processing difficulty will be encountered.
- II The considerable receiving area (Fig. 14(a-c)) of the absorber also relieves the urgent demand for angular stability of the meta-lens, providing more room for optimizing the large incident angle sunlight convergence performance according to the boundary conditions in Eq. (12–15) for a wide FOV meta-lens design. In addition, considering that low and middle latitude regions are more suitable for solar energy harvesting than the high region, the incident angle variation of sunlight introduced by the Earth's rotation is more critical than that induced by revolution around the sun. Therefore, the meta-lens with axisymmetric property shown in Fig. 14(a-c) is an appropriate choice for producing linear foci and maintaining the shift along the heat-collecting pipe from sunrise to sunset. Besides the relaxed design principle, the symmetrical structure shows another remarkable advantage in large-scale fabrication via an optimized processing strategy (details in the following section).
- III Currently, exploitation of solar energy is based on the accumulative effect, leading to the large-size requirement of the meta-lens. The fabrication methods summarized in Section 6 can only transfer the same small-sized meta-lens to different locations of a large-area wafer, but cannot complete the entire plane preparation.

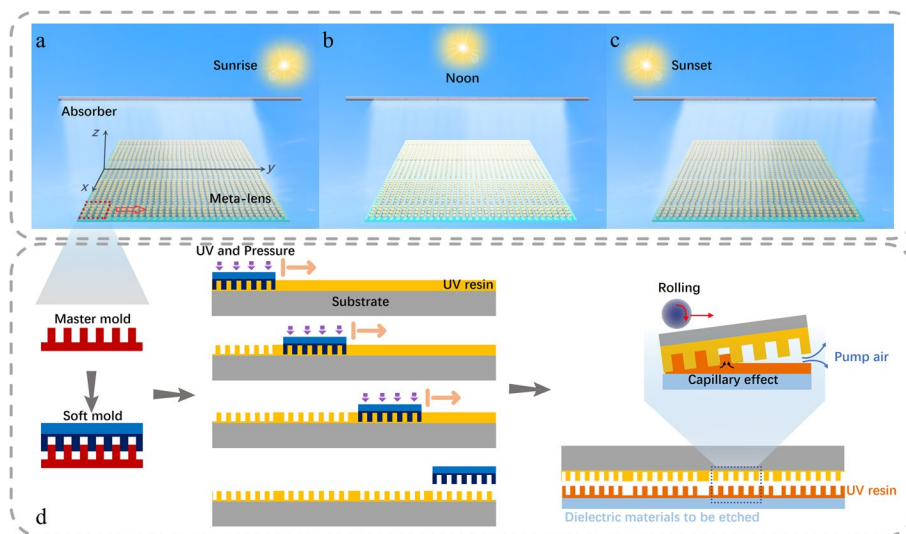


**Fig. 14** a–c Linear-focusing meta-lens and its focal performance vary from sunset to sunrise. **d** Fabrication process for the large-scale meta-lens using NIL technology

Hence, it is necessary to develop large-area fabrication and mass-production methods to replace their traditional counterparts. Therefore, several alternative techniques [179, 242–244], such as two/multi-photon lithography and nanoimprinting lithography (NIL) [245–247] have been proposed to address these problems, of which high-precise nanoimprinting can easily transfer predesigned large-scale patterns to the resist layer, as in lithography, with enormous potential for low-cost, large-sized solar concentrator fabrication.

With regards to the line-focusing meta-lens illustrated in Fig. 14(a–c), two features are convenient in terms of the NIL process: I. The required phase gradient for focusing is only orthogonal to the absorption tube (along  $x$ -direction in Fig. 14(a)), and the corresponding nanostructures are symmetric with respect to the  $y$ -axis (Fig. 14(a)); II. Nanostructures along the  $y$ -direction are identical. Depending on these characteristics, a promising method is proposed in Fig. 14(d) for scale-up fabrication of the metasurface-based concentrators: First, based on the selected nanostructure array (red dashed box in Fig. 14(a)), a master mold is fabricated via EBL. Then, this mold is transferred as a soft mold (namely, a working mold) for the succeeding processes (left side of Fig. 14(d)). The working mold, which supports reuse, can help to avoid damage to the high-cost master mold. In the following, considering feature II of the meta-lens, the original master mold can be expanded along the  $y$ -direction (red arrow in Fig. 14(a)) using flash stepping nanoimprinting technology [248–250] (middle of Fig. 14(d)). Subsequently, the magnified pattern can be successfully transferred to the resin (right side of Fig. 14(d)) by utilizing the improved large-scale nanoimprinting (top-right of Fig. 14(d)). Different from the traditional NIL, the modified approach causes a negative pressure between the working mold and the resin by pumping out the extra gas, which can assist in quickly and actively drawing the resin into the structural gaps, enhancing the capillary effect, and making the nanostructure filling more completely. Finally, the meta-lens fabrication process will be

completed by repeating the aforementioned procedures. In addition, due to feature I of the meta-lens, the expected workload can be further reduced in half. There are still some problems associated with this fabrication method such as the stitching error generated during flash stepping nanoimprinting, large-scale etching technologies, etc., which urgently need to be addressed. Hopefully, more researchers will be inspired by the desire to explore these techniques, and exploit new possibilities in the future.

In general, there is still a long way before solar harvest systems that utilize novel meta-lenses are finally developed. However, it is likely that with continuous advances in meta-technology and processing capability, macro applications will become a reality in the near future, resulting in a new energy revolution.

#### Abbreviations

CSP	Concentrated solar power
VR	Virtual reality
NA	Numerical aperture
FL	Focal length
AR	Aspect ratio
PB	Pancharatnam-Berry
1D	One-dimensional
2D	Two-dimensional
CP	Circular polarization
IR	Infrared
NIR	Near-infrared
Nb <sub>2</sub> O <sub>5</sub>	Niobium pentoxide
HfO <sub>2</sub>	Hafnium oxide
AlN	Aluminum nitride
UV	Ultraviolet
DUV	deep-UV
TiO <sub>2</sub>	Titanium dioxide
Si <sub>3</sub> N <sub>4</sub>	Silicon nitride
SiN <sub>x</sub>	Silicon-rich nitride
c-Si	Crystalline silicon
GaN	Gallium nitride
Ge	Germanium
p-Si	Poly-silicon
a-Si	Amorphous silicon
PbTe	Lead telluride
LP	Linear-polarization
HCTA	High-contrast transmit array
EBL	Electron-beam lithography
FIB	Focused ion beam
RIE	Reactive ion etching
SiO <sub>2</sub>	Fused-silica
ACS	American Chemical Society
NPG	Nature Publication Group
FWHM	Full width at half maximum
FOV	Field of view
ALD	Atomic layer deposition
IRUE	Integrated-resonant unit element
TE	Transverse electric
TM	Transverse magnetic
Cl <sub>2</sub>	Chlorine
Cr	Chrome
CHF <sub>3</sub>	Trifluoromethane
Ar	Argon
SEM	Scanning electron microscope
Mat	Material
Pol	Polarization
R	Reflection type
T	Transmission type
WL	Wavelength
Eff	Efficiency
Diam	Diameter
Ref	Reference

### Acknowledgements

This work was supported in part by the National Key Research and Development Program of China (2020YFA0710100), the National Natural Science Foundation of China (61731010), the Fundamental Research Funds for the Central Universities (WUT: 2021IVA064), the Foundation from Guangxi Key Laboratory of Optoelectronic Information Processing (GD21203).

### Authors' contributions

Methodology, CZ, and JG; writing—original draft preparation, CZ; writing—review and editing, CZ, YZ, YQ, LX, and JG; supervision, JG. All authors read and approved the final manuscript.

### Funding

National Key Research and Development Program of China (2020YFA0710100), the National Natural Science Foundation of China (61731010), the Fundamental Research Funds for the Central Universities (WUT: 2021IVA064), the Foundation from Guangxi Key Laboratory of Optoelectronic Information Processing (GD21203).

### Availability of data and materials

Data sharing is not applicable to this article as no new datasets were created in this review.

### Declarations

#### Competing interests

The authors declare no competing financial interests.

Received: 8 August 2022 Revised: 28 October 2022 Accepted: 8 November 2022

Published online: 29 November 2022

### References

1. Goel A, Manik G. Solar thermal system—an insight into parabolic trough solar collector and its modeling. *Renewable Energy Systems*: Elsevier; 2021. p. 309–37.
2. Dudley B. BP statistical review of world energy. BP Stat Rev London, UK. 2018;2018(6):00116.
3. by fuel type-Exajoules, C. bp Statistical Review of World Energy. 2006
4. Shafiee S, Topal E. When will fossil fuel reserves be diminished? *Energy Policy*. 2009;37(1):181–9.
5. Da Rosa AV, Ordóñez JC. *Fundamentals of renewable energy processes*: Academic; 2021.
6. World Energy Council. *World energy resources report*; 2016.
7. Twidell J. *Renewable energy resources*: Routledge; 2021.
8. Kamran M, Fazal MR. *Fundamentals of renewable energy systems*: Academic; 2021.
9. Mekhilef S, Saidur R, Safari A. A review on solar energy use in industries. *Renew Sust Energy Rev*. 2011;15(4):1777–90.
10. Sherwood AN, Nikolic M, Humphrey JW, et al. *Greek and Roman technology: a sourcebook: annotated translations of Greek and Latin texts and documents*: Routledge; 2003.
11. Plantzos D. Crystals and lenses in the Graeco-Roman world. *Am J Archaeol*. 1997;101(3):451–64.
12. Meijer F. *A history of seafaring in the classical world (Routledge revivals)*: Routledge; 2014.
13. Tian Y, Zhao C-Y. A review of solar collectors and thermal energy storage in solar thermal applications. *Appl Energy*. 2013;104:538–53.
14. Romero M, Steinfeld A. Concentrating solar thermal power and thermochemical fuels. *Energy Environ Sci*. 2012;5(11):9234–45.
15. Lovegrove K, Stein W. *Concentrating solar power technology: principles. Developments and Applications*: Woodhead Publishing; 2012.
16. Nation DD, Hegggs PJ, Dixon-Hardy DW. Modelling and simulation of a novel electrical energy storage (EES) receiver for solar parabolic trough collector (PTC) power plants. *Appl Energy*. 2017;195:950–73.
17. Hossain M, Saidur R, Fayaz H, et al. Review on solar water heater collector and thermal energy performance of circulating pipe. *Renew Sust Energy Rev*. 2011;15(8):3801–12.
18. Hossain E, Petrovic S. *Solar thermal energy*. In: *Renewable energy crash course*: Springer; 2021. p. 61–8.
19. Hachicha AA, Yousef BA, Said Z, et al. A review study on the modeling of high-temperature solar thermal collector systems. *Renew Sust Energy Rev*. 2019;112:280–98.
20. Blanco M. *Advances in concentrating solar thermal research and technology*: Woodhead Publishing; 2016.
21. Islam MT, Huda N, Abdullah A, et al. A comprehensive review of state-of-the-art concentrating solar power (CSP) technologies: current status and research trends. *Renew Sust Energy Rev*. 2018;91:987–1018.
22. Esen M. Thermal performance of a solar cooker integrated vacuum-tube collector with heat pipes containing different refrigerants. *Sol Energy*. 2004;76(6):751–7.
23. Esen M, Esen H. Experimental investigation of a two-phase closed thermosyphon solar water heater. *Sol Energy*. 2005;79(5):459–68.
24. Alam T, Saini R, Saini J. Heat transfer enhancement due to V-shaped perforated blocks in a solar air heater duct. In: *Applied mechanics and materials*; 2014. p. 125–9. *Trans Tech Publ*.
25. Alam T, Kim M-H. Numerical study on thermal hydraulic performance improvement in solar air heater duct with semi ellipse shaped obstacles. *Energy*. 2016;112:588–98.
26. Esen M, Yuksel T. Experimental evaluation of using various renewable energy sources for heating a greenhouse. *Energy Build*. 2013;65:340–51.

27. Al-harashsheh M, Abu-Arabi M, Mousa H, et al. Solar desalination using solar still enhanced by external solar collector and PCM. *Appl Therm Eng*. 2018;128:1030–40.
28. Garg HP, Mullick S, Bhargava VK. *Solar thermal energy storage*: Springer Science & Business Media; 2012.
29. Mehrali M, Johan E, Shahi M, et al. Simultaneous solar-thermal energy harvesting and storage via shape stabilized salt hydrate phase change material. *Chem Eng J*. 2021;405:126624.
30. Li Y, Chen Y, Huang X, et al. Anisotropy-functionalized cellulose-based phase change materials with reinforced solar-thermal energy conversion and storage capacity. *Chem Eng J*. 2021;415:129086.
31. Sharma V, Kumar A, Sastry O, et al. Performance assessment of different solar photovoltaic technologies under similar outdoor conditions. *Energy*. 2013;58:511–8.
32. Grätzel M. Solar energy conversion by dye-sensitized photovoltaic cells. *Inorg Chem*. 2005;44(20):6841–51.
33. Izquierdo S, Montañés C, Dopazo C, et al. Analysis of CSP plants for the definition of energy policies: the influence on electricity cost of solar multiples, capacity factors and energy storage. *Energy Policy*. 2010;38(10):6215–21.
34. Yilmaz IH, Mwesigye A. Modeling, simulation and performance analysis of parabolic trough solar collectors: a comprehensive review. *Appl Energy*. 2018;225:135–74.
35. Bellos E, Tzivanidis C. Alternative designs of parabolic trough solar collectors. *Prog Energy Combust Sci*. 2019;71:81–117.
36. Rasul M. Clean energy for sustainable development: comparisons and contrasts of new approaches: Academic; 2016.
37. Suman S, Khan MK, Pathak M. Performance enhancement of solar collectors—a review. *Renew Sust Energy Rev*. 2015;49:192–210.
38. Kalogirou SA. Solar thermal collectors and applications. *Prog Energy Combust Sci*. 2004;30(3):231–95.
39. Zayed ME, Zhao J, Elsheikh AH, et al. Applications of cascaded phase change materials in solar water collector storage tanks: a review. *Sol Energy Mater Sol Cells*. 2019;199:24–49.
40. Mancini T, Heller P, Butler B, et al. Dish-Stirling systems: An overview of development and status. *J Sol Energy Eng*. 2003;125(2):135–51.
41. Stine W, Diver R. A compendium of solar dish Stirling technology. Report SAND 937026. Albuquerque: Sandia National Laboratories; 1994.
42. Kearney A. Solar thermal electricity 2025. Clean electricity on demand: Attractive STE cost stabilize energy production; 2010.
43. Ho CK, Iverson BD. Review of high-temperature central receiver designs for concentrating solar power. *Renew Sust Energy Rev*. 2014;29:835–46.
44. Behar O, Khellaf A, Mohammedi K. A review of studies on central receiver solar thermal power plants. *Renew Sust Energy Rev*. 2013;23:12–39.
45. Yogev A, Kribus A, Epstein M, et al. Solar “tower reflector” systems: a new approach for high-temperature solar plants. *Int J Hydrog Energy*. 1998;23(4):239–45.
46. Mills D. Advances in solar thermal electricity technology. *Sol Energy*. 2004;76(1-3):19–31.
47. Yu N, Genevet P, Kats MA, et al. Light propagation with phase discontinuities: generalized laws of reflection and refraction. *Science*. 2011;334(6054):333–7.
48. Yu N, Capasso F. Flat optics with designer metasurfaces. *Nat Mater*. 2014;13(2):139–50.
49. Chen H-T, Taylor AJ, Yu N. A review of metasurfaces: physics and applications. *Rep Prog Phys*. 2016;79(7):076401.
50. Ding F, Pors A, Bozhevolnyi SI. Gradient metasurfaces: a review of fundamentals and applications. *Rep Prog Phys*. 2017;81(2):026401.
51. Genevet P, Capasso F, Aieta F, et al. Recent advances in planar optics: from plasmonic to dielectric metasurfaces. *Optica*. 2017;4(1):139–52.
52. Meinzer N, Barnes WL, Hooper IR. Plasmonic meta-atoms and metasurfaces. *Nat Photonics*. 2014;8(12):889–98.
53. Chen WT, Zhu AY, Capasso F. Flat optics with dispersion-engineered metasurfaces. *Nat Rev Mater*. 2020;5(8):604–20.
54. Hsiao HH, Chu CH, Tsai DP. Fundamentals and applications of metasurfaces. *Small Methods*. 2017;1(4):1600064.
55. Yoon G, Tanaka T, Zentgraf T, et al. Recent progress on metasurfaces: applications and fabrication. *J Phys D Appl Phys*. 2021;54(38):383002.
56. Luo X, Tsai D, Gu M, et al. Extraordinary optical fields in nanostructures: from sub-diffraction-limited optics to sensing and energy conversion. *Chem Soc Rev*. 2019;48(8):2458–94.
57. Lee S-Y, Kim K, Kim S-J, et al. Plasmonic meta-slit: shaping and controlling near-field focus. *Optica*. 2015;2(1):6–13.
58. Chen X, Zhang Y, Huang L, et al. Ultrathin metasurface laser beam shaper. *Adv Optical Mat*. 2014;2(10):978–82.
59. Sun S, Yang K-Y, Wang C-M, et al. High-efficiency broadband anomalous reflection by gradient meta-surfaces. *Nano Lett*. 2012;12(12):6223–9.
60. Walther B, Helgert C, Rockstuhl C, et al. Photonics: spatial and spectral light shaping with Metamaterials. *Adv Mater*. 2012;24(47):6251.
61. Zheng G, Mühlenbernd H, Kenney M, et al. Metasurface holograms reaching 80% efficiency. *Nat Nanotechnol*. 2015;10(4):308–12.
62. Sun S, He Q, Xiao S, et al. Gradient-index meta-surfaces as a bridge linking propagating waves and surface waves. *Nat Mater*. 2012;11(5):426–31.
63. Chen K, Feng Y, Monticone F, et al. A reconfigurable active Huygens’ metalens. *Adv Mater*. 2017;29(17):1606422.
64. Cui TJ, Qi MQ, Wan X, et al. Coding metamaterials, digital metamaterials and programmable metamaterials. *Light Sci Appl*. 2014;3(10):e218.
65. Kamali SM, Arbabi E, Arbabi A, et al. Angle-multiplexed metasurfaces: encoding independent wavefronts in a single metasurface under different illumination angles. *Physical Review X*. 2017;7(4):041056.
66. Wang L, Kruk S, Tang H, et al. Grayscale transparent metasurface holograms. *Optica*. 2016;3(12):1504–5.
67. Genevet P, Capasso F. Holographic optical metasurfaces: a review of current progress. *Rep Prog Phys*. 2015;78(2):024401.
68. Deng ZL, Deng J, Zhuang X, et al. Diatomic metasurface for vectorial holography. *Nano Lett*. 2018;18(5):2885–92.

69. Ding X, Monticone F, Zhang K, et al. Ultrathin Pancharatnam–Berry metasurface with maximal cross-polarization efficiency. *Adv Mater.* 2015;27(7):1195–200.
70. Yu N, Aieta F, Genevet P, et al. A broadband, background-free quarter-wave plate based on plasmonic metasurfaces. *Nano Lett.* 2012;12(12):6328–33.
71. Perez-Palomino G, Page JE, Arrebola M, et al. A design technique based on equivalent circuit and coupler theory for broadband linear to circular polarization converters in reflection or transmission mode. *IEEE Trans Antennas Propag.* 2018;66(5):2428–38.
72. Grady NK, Heyes JE, Chowdhury DR, et al. Terahertz metamaterials for linear polarization conversion and anomalous refraction. *Science.* 2013;340(6138):1304–7.
73. Rodríguez-Fortuño FJ, Marino G, Ginzburg P, et al. Near-field interference for the unidirectional excitation of electromagnetic guided modes. *Science.* 2013;340(6130):328–30.
74. Pors A, Nielsen MG, Bernardin T, et al. Efficient unidirectional polarization-controlled excitation of surface plasmon polaritons. *Light: Sci App.* 2014;3(8):e197.
75. Lin J, Mueller JB, Wang Q, et al. Polarization-controlled tunable directional coupling of surface plasmon polaritons. *Science.* 2013;340(6130):331–4.
76. Wu L, Oudich M, Cao W, et al. Routing acoustic waves via a metamaterial with extreme anisotropy. *Phys Rev Appl.* 2019;12(4):044011.
77. Cao WK, Wu LT, Zhang C, et al. Asymmetric transmission of acoustic waves in a waveguide via gradient index metamaterials. *Sci Bull.* 2019;64(12):808–13.
78. Li X, Xiao S, Cai B, et al. Flat metasurfaces to focus electromagnetic waves in reflection geometry. *Opt Lett.* 2012;37(23):4940–2.
79. Pors A, Nielsen MG, Eriksen RL, et al. Broadband focusing flat mirrors based on plasmonic gradient metasurfaces. *Nano Lett.* 2013;13(2):829–34.
80. Shen K, Duan Y, Ju P, et al. On-chip optical levitation with a metalens in vacuum. *Optica.* 2021;8(11):1359–62.
81. Zhang C, Cao WK, Wu LT, et al. A reconfigurable active acoustic metalens. *Appl Phys Lett.* 2021;118(13):133502.
82. Yang W, Chen K, Zheng Y, et al. Angular-adaptive reconfigurable spin-locked Metasurface Retroreflector. *Adv Sci.* 2021;8(21):2100885.
83. Karvounis A, Gholipour B, MacDonald KF, et al. All-dielectric phase-change reconfigurable metasurface. *Appl Phys Lett.* 2016;109(5):051103.
84. Huang C, Yang J, Wu X, et al. Reconfigurable metasurface cloak for dynamical electromagnetic illusions. *ACS Photonics.* 2017;5(5):1718–25.
85. Lu X, Dong B, Zhu H, et al. Two-channel vo2 memory meta-device for terahertz waves. *Nanomaterials.* 2021;11(12):3409.
86. Cao WK, Zhang C, Wu LT, et al. Tunable acoustic metasurface for three-dimensional wave manipulations. *Phys Rev Appl.* 2021;15(2):024026.
87. Dong B, Zhang C, Guo G, et al. BST-silicon hybrid terahertz meta-modulator for dual-stimuli-triggered opposite transmission amplitude control. *Nanophotonics.* 2022;11(9):2075–83.
88. Lee D, Gwak J, Badloe T, et al. Metasurfaces-based imaging and applications: from miniaturized optical components to functional imaging platforms. *Nanoscale Adv.* 2020;2(2):605–25.
89. Li Z, Lin P, Huang Y-W, et al. Meta-optics achieves RGB-achromatic focusing for virtual reality. *Sci Adv.* 2021;7(5):eabe4458.
90. Hoffman DM, Girshick AR, Akeley K, et al. Vergence–accommodation conflicts hinder visual performance and cause visual fatigue. *J Vis.* 2008;8(3):33.
91. Liu S, Li Y, Zhou P, et al. A multi-plane optical see-through head mounted display design for augmented reality applications. *J Soc Inf Disp.* 2016;24(4):246–51.
92. Lee G-Y, Hong J-Y, Hwang S, et al. Metasurface eyepiece for augmented reality. *Nat Commun.* 2018;9(1):1–10.
93. Jang C, Bang K, Li G, et al. Holographic near-eye display with expanded eye-box. *ACM Transact Graphics (TOG).* 2018;37(6):1–14.
94. Lee S, Jo Y, Yoo D, et al. Tomographic near-eye displays. *Nat Commun.* 2019;10(1):1–10.
95. Lalanne P, Astilean S, Chavel P, et al. Blazed binary subwavelength gratings with efficiencies larger than those of conventional échelette gratings. *Opt Lett.* 1998;23(14):1081–3.
96. Liang H, Martins A, Borges B-HV, et al. High performance metalenses: numerical aperture, aberrations, chromaticity, and trade-offs. *Optica.* 2019;6(12):1461–70.
97. Decker M, Staude I, Falkner M, et al. High-efficiency dielectric Huygens’ surfaces. *Adv Optic Mater.* 2015;3(6):813–20.
98. Ni X, Ishii S, Kildishev AV, et al. Ultra-thin, planar, Babinet-inverted plasmonic metalenses. *Light: Sci App.* 2013;2(4):e72.
99. Akahane Y, Asano T, Song B-S, et al. High-Q photonic nanocavity in a two-dimensional photonic crystal. *Nature.* 2003;425(6961):944–7.
100. Liu W, Li Z, Cheng H, et al. Metasurface enabled wide-angle Fourier lens. *Adv Mater.* 2018;30(23):1706368.
101. Koshelev K, Kivshar Y. Dielectric resonant metaphotonics. *ACS Photonics.* 2020;8(1):102–12.
102. Yang B, Liu W, Li Z, et al. Ultrahighly saturated structural colors enhanced by multipolar-modulated metasurfaces. *Nano Lett.* 2019;19(7):4221–8.
103. Porto J, Garcia-Vidal F, Pendry J. Transmission resonances on metallic gratings with very narrow slits. *Phys Rev Lett.* 1999;83(14):2845.
104. Li J, Chen Y, Hu Y, et al. Magnesium-based metasurfaces for dual-function switching between dynamic holography and dynamic color display. *ACS Nano.* 2020;14(7):7892–8.
105. Chen Y, Duan X, Matuschek M, et al. Dynamic color displays using stepwise cavity resonators. *Nano Lett.* 2017;17(9):5555–60.
106. Yang Z, Chen Y, Zhou Y, et al. Microscopic interference full-color printing using grayscale-patterned Fabry–Perot resonance cavities. *Adv Optical Mat.* 2017;5(10):1700029.

107. Wang Y, Zheng M, Ruan Q, et al. Stepwise-nanocavity-assisted transmissive color filter array microprints. *Research*. 2018;2018:8109054.
108. Verslegers L, Catrysse PB, Yu Z, et al. Planar lenses based on nanoscale slit arrays in a metallic film. *Nano Lett*. 2009;9(1):235–8.
109. Kumar K, Duan H, Hegde RS, et al. Printing colour at the optical diffraction limit. *Nat Nanotechnol*. 2012;7(9):557–61.
110. Segal N, Keren-Zur S, Hendler N, et al. Controlling light with metamaterial-based nonlinear photonic crystals. *Nat Photonics*. 2015;9(3):180–4.
111. Huang X, Lai Y, Hang ZH, et al. Dirac cones induced by accidental degeneracy in photonic crystals and zero-refractive-index materials. *Nat Mater*. 2011;10(8):582–6.
112. Yang J, Ghimire I, Wu PC, et al. Photonic crystal fiber metalens. *Nanophotonics*. 2019;8(3):443–9.
113. Chang-Hasnain CJ, Yang W. High-contrast gratings for integrated optoelectronics. *Adv Opt Photon*. 2012;4(3):379–440.
114. Lin D, Fan P, Hasman E, et al. Dielectric gradient metasurface optical elements. *Science*. 2014;345(6194):298–302.
115. Huang MC, Zhou Y, Chang-Hasnain CJ. A surface-emitting laser incorporating a high-index-contrast subwavelength grating. *Nat Photonics*. 2007;1(2):119–22.
116. Zhou H, Chen L, Shen F, et al. Broadband achromatic metalens in the midinfrared range. *Phys Rev Appl*. 2019;11(2):024066.
117. Khorasaninejad M, Capasso F. Broadband multifunctional efficient meta-gratings based on dielectric waveguide phase shifters. *Nano Lett*. 2015;15(10):6709–15.
118. Khorasaninejad M, Crozier KB. Silicon nanofin grating as a miniature chirality-distinguishing beam-splitter. *Nat Commun*. 2014;5(1):1–6.
119. Khorasaninejad M, Zhu AY, Roques-Carmes C, et al. Polarization-insensitive metalenses at visible wavelengths. *Nano Lett*. 2016;16(11):7229–34.
120. Devlin RC, Khorasaninejad M, Chen WT, et al. Broadband high-efficiency dielectric metasurfaces for the visible spectrum. *Proc Natl Acad Sci*. 2016;113(38):10473–8.
121. Maguid E, Yulevich I, Yannai M, et al. Multifunctional interleaved geometric-phase dielectric metasurfaces. *Light: Sci App*. 2017;6(8):e17027-e.
122. Mueller JB, Rubin NA, Devlin RC, et al. Metasurface polarization optics: independent phase control of arbitrary orthogonal states of polarization. *Phys Rev Lett*. 2017;118(11):113901.
123. Pancharatnam S. Generalized theory of interference and its applications. In: *Proceedings of the Indian Academy of Sciences-section a*, 1956. Abstract 6: Springer. p. 398–417.
124. Berry MV. The adiabatic phase and Pancharatnam's phase for polarized light. *J Mod Opt*. 1987;34(11):1401–7.
125. Xie X, Pu M, Jin J, et al. Generalized Pancharatnam-Berry phase in rotationally symmetric meta-atoms. *Phys Rev Lett*. 2021;126(18):183902.
126. Liu W, Li Z, Cheng H, et al. Dielectric resonance-based optical metasurfaces: from fundamentals to applications. *IScience*. 2020;23(12):101868.
127. Brown BR, Lohmann AW. Complex spatial filtering with binary masks. *Appl Opt*. 1966;5(6):967–9.
128. Lohmann AW, Paris DP. Binary Fraunhofer holograms, generated by computer. *Appl Opt*. 1967;6(10):1739–48.
129. Min C, Liu J, Lei T, et al. Plasmonic nano-slits assisted polarization selective detour phase meta-hologram. *Laser Photonics Rev*. 2016;10(6):978–85.
130. Zhang K, Wang Y, Burokur SN, et al. Generating dual-polarized vortex beam by detour phase: from phase gradient metasurfaces to metagratings. *IEEE Transact Microwave Theory Techn*. 2021;70(1):200–9.
131. Lin J, Genevet P, Kats MA, et al. Nanostructured holograms for broadband manipulation of vector beams. *Nano Lett*. 2013;13(9):4269–74.
132. Xie Z, Lei T, Si G, et al., Min C, Liu J, et al. Meta-holograms with full parameter control of wavefront over a 1000 nm bandwidth. *ACS Photonics*. 2017;4(9):2158–64.
133. Poon TC. *Digital holography and three-dimensional display: principles and applications*: Springer Science & Business Media; 2006.
134. Chen X, Huang L, Mühlenbernd H, et al. Dual-polarity plasmonic metalens for visible light. *Nat Commun*. 2012;3(1):1–6.
135. Wang W, Guo Z, Li R, et al. Ultra-thin, planar, broadband, dual-polarity plasmonic metalens. *Photon Res*. 2015;3(3):68–71.
136. Luo X. Plasmonic metalens for nanofabrication. *Natl Sci Rev*. 2018;5(2):137–8.
137. Williams C, Montelongo Y, Wilkinson TD. Plasmonic Metalens for narrowband dual-focus imaging. *Adv Optical Mat*. 2017;5(24):1700811.
138. Chen X, Huang L, Mühlenbernd H, et al. Reversible three-dimensional focusing of visible light with ultrathin Plasmonic flat lens. *Adv Optical Mat*. 2013;1(7):517–21.
139. Schlickriede C, Waterman N, Reineke B, et al. Imaging through nonlinear metalens using second harmonic generation. *Adv Mater*. 2018;30(8):1703843.
140. Francesco A, Genevet P, Kats MA, et al. Aberration-free ultrathin flat lenses and axicons at telecom wavelengths based on plasmonic metasurfaces. *Nano Lett*. 2012;12(9):4932–6.
141. Avayu O, Almeida E, Prior Y, et al. Composite functional metasurfaces for multispectral achromatic optics. *Nat Commun*. 2017;8(1):1–7.
142. Jahani S, Jacob Z. All-dielectric metamaterials. *Nat Nanotechnol*. 2016;11(1):23–36.
143. Kuznetsov AI, Miroshnichenko AE, Brongersma ML, et al. Optically resonant dielectric nanostructures. *Science*. 2016;354(6314):aag2472.
144. Cheng J, Jafar-Zanjani S, Mosallaei H. All-dielectric ultrathin conformal metasurfaces: lensing and cloaking applications at 532 nm wavelength. *Sci Rep*. 2016;6(1):1–10.
145. Huang K, Deng J, Leong HS, et al. Ultraviolet Metasurfaces of  $\approx 80\%$  efficiency with antiferromagnetic resonances for optical Vectorial anti-counterfeiting. *Laser Photonics Rev*. 2019;13(5):1800289.



146. Zhang C, Divitt S, Fan Q, et al. Low-loss metasurface optics down to the deep ultraviolet region. *Light: Sci App.* 2020;9(1):1–10.
147. Hemmatyar O, Abdollahramezani S, Kiarashinejad Y, et al. Full color generation with Fano-type resonant hfo 2 nanopillars designed by a deep-learning approach. *Nanoscale.* 2019;11(44):21266–74.
148. Guo L, Hu Z, Wan R, et al. Design of aluminum nitride metalens for broadband ultraviolet incidence routing. *Nano-photonics.* 2019;8(1):171–80.
149. Guo L, Xu S, Wan R, et al. Design of aluminum nitride metalens in the ultraviolet spectrum. *J Nanophoton.* 2018;12(4):043513.
150. Khorasaninejad M, Chen WT, Devlin RC, et al. Metalenses at visible wavelengths: diffraction-limited focusing and subwavelength resolution imaging. *Science.* 2016;352(6290):1190–4.
151. Chen WT, Zhu AY, Sisler J, et al. A broadband achromatic polarization-insensitive metalens consisting of anisotropic nanostructures. *Nat Commun.* 2019;10(1):1–7.
152. Chen WT, Zhu AY, Sanjeev V, et al. A broadband achromatic metalens for focusing and imaging in the visible. *Nat Nanotechnol.* 2018;13(3):220–6.
153. Groever B, Chen WT, Capasso F. Meta-lens doublet in the visible region. *Nano Lett.* 2017;17(8):4902–7.
154. Khorasaninejad M, Shi Z, Zhu AY, et al. Achromatic metalens over 60 nm bandwidth in the visible and metalens with reverse chromatic dispersion. *Nano Lett.* 2017;17(3):1819–24.
155. Chen WT, Zhu AY, Khorasaninejad M, et al. Immersion meta-lenses at visible wavelengths for nanoscale imaging. *Nano Lett.* 2017;17(5):3188–94.
156. Poulton CV, Byrd MJ, Raval M, et al. Large-scale silicon nitride nanophotonic phased arrays at infrared and visible wavelengths. *Opt Lett.* 2017;42(1):21–4.
157. Fan ZB, Shao ZK, Xie MY, et al. Silicon nitride metalenses for close-to-one numerical aperture and wide-angle visible imaging. *Phys Rev Appl.* 2018;10(1):014005.
158. Ye M, Ray V, Wu D, et al. Metalens with artificial focus pattern. *IEEE Photon Technol Lett.* 2020;32(5):251–4.
159. Park CS, Koirala I, Gao S, et al. Structural color filters based on an all-dielectric metasurface exploiting silicon-rich silicon nitride nanodisks. *Opt Express.* 2019;27(2):667–79.
160. Liang H, Lin Q, Xie X, et al. Ultrahigh numerical aperture metalens at visible wavelengths. *Nano Lett.* 2018;18(7):4460–6.
161. Sell D, Yang J, Doshay S, et al. Visible light metasurfaces based on single-crystal silicon. *Acs Photonics.* 2016;3(10):1919–25.
162. Zhou Z, Li J, Su R, et al. Efficient silicon metasurfaces for visible light. *Acs Photonics.* 2017;4(3):544–51.
163. Emani NK, Khaidarov E, Paniagua-Domínguez R, et al. High-efficiency and low-loss gallium nitride dielectric metasurfaces for nanophotonics at visible wavelengths. *Appl Phys Lett.* 2017;111(22):221101.
164. Chen BH, Wu PC, Su V-C, et al. GaN metalens for pixel-level full-color routing at visible light. *Nano Lett.* 2017;17(10):6345–52.
165. Wang S, Wu PC, Su V-C, et al. A broadband achromatic metalens in the visible. *Nat Nanotechnol.* 2018;13(3):227–32.
166. Grinblat G, Li Y, Nielsen MP, et al. Efficient third harmonic generation and nonlinear subwavelength imaging at a higher-order anapole mode in a single germanium nanodisk. *ACS Nano.* 2017;11(1):953–60.
167. Wang A, Chen Z, Dan Y. Planar metalenses in the mid-infrared. *AIP Adv.* 2019;9(8):085327.
168. Dong Z, Ho J, Yu YF, et al. Printing beyond sRGB color gamut by mimicking silicon nanostructures in free-space. *Nano Lett.* 2017;17(12):7620–8.
169. Shrestha S, Overvig AC, Lu M, et al. Broadband achromatic dielectric metalenses. *Light: Sci App.* 2018;7(1):1–11.
170. Li J, Wang Y, Liu S, et al. Dielectric metasurfaces for complete control of phase and polarization with subwavelength spatial resolution and high transmission. Largest aperture metalens of high numerical aperture and polarization independence for long-wavelength infrared imaging. *Opt Express.* 2022;30(16):28882–91.
171. Shan X, Li Z, Li J, et al. Broadband continuous achromatic and super-dispersive metalens in near-infrared band. *J Appl Phys.* 2021;131(2):023103.
172. Arbabi A, Horie Y, Bagheri M, et al. Dielectric metasurfaces for complete control of phase and polarization with subwavelength spatial resolution and high transmission. *Nat Nanotechnol.* 2015;10(11):937–43.
173. Zhang L, Ding J, Zheng H, et al. Ultra-thin high-efficiency mid-infrared transmissive Huygens meta-optics. *Nat Commun.* 2018;9(1):1–9.
174. Shalaginov MY, An S, Yang F, et al. Single-element diffraction-limited fisheye metalens. *Nano Lett.* 2020;20(10):7429–37.
175. Arbabi A, Horie Y, Ball AJ, et al. Subwavelength-thick lenses with high numerical apertures and large efficiency based on high-contrast transmitarrays. *Nat Commun.* 2015;6(1):1–6.
176. Majka M, Majka TM. Healthy light source; 2013.
177. Rodziewicz T, Rajfur M, Teneta J, et al. Modelling and analysis of the influence of solar spectrum on the efficiency of photovoltaic modules. *Energy Rep.* 2021;7:565–74.
178. Balli F, Sultan M, Lami SK, et al. A hybrid achromatic metalens. *Nat Commun.* 2020;11(1):1–8.
179. Yoon G, Kim K, Kim S-U, et al. Printable nanocomposite metalens for high-contrast near-infrared imaging. *ACS Nano.* 2021;15(1):698–706.
180. Li B, Piyawattanametha W, Qiu Z. Metalens-based miniaturized optical systems. *Micromachines.* 2019;10(5):310.
181. She A, Zhang S, Shian S, et al. Adaptive metalenses with simultaneous electrical control of focal length, astigmatism, and shift. *Sci Adv.* 2018;4(2):eaap9957.
182. Bayati E, Zhan A, Colburn S, et al. Role of refractive index in metalens performance. *Appl Opt.* 2019;58(6):1460–6.
183. Wu Z, Dong F, Zhang S, et al. Broadband dielectric metalens for polarization manipulating and superoscillation focusing of visible light. *Acs Photonics.* 2019;7(1):180–9.
184. Chen C, Song W, Chen JW, et al. Spectral tomographic imaging with aplanatic metalens. *Light: Sci App.* 2019;8(1):1–8.

185. Fan ZB, Qiu HY, Zhang HL, et al. A broadband achromatic metalens array for integral imaging in the visible. *Light: Sci Appl.* 2019;8(1):1–10.
186. Uenoyama S, Ota R. 40x 40 Metalens Array for improved silicon photomultiplier performance. *ACS Photonics.* 2021;8(6):1548–55.
187. Chang WH, Lin JH, Kuan CH, et al. Generation of concentric space-variant linear polarized light by dielectric metalens. *Nano Lett.* 2020;21(1):562–8.
188. Kanwal S, Wen J, Yu B, et al. High-efficiency, broadband, near diffraction-limited, dielectric metalens in ultraviolet spectrum. *Nanomaterials.* 2020;10(3):490.
189. Ali F, Aksu S. A hybrid broadband metalens operating at ultraviolet frequencies. *Sci Rep.* 2021;11(1):1–8.
190. Kanwal S, Wen J, Yu B, et al. Polarization insensitive, broadband, near diffraction-limited metalens in ultraviolet region. *Nanomaterials.* 2020;10(8):1439.
191. Hu M, Wei Y, Cai H, et al. Polarization-insensitive and achromatic metalens at ultraviolet wavelengths. *J Nanophoton.* 2019;13(3):036015.
192. Liu M, Xu N, Wang B, et al. Polarization independent and broadband achromatic metalens in ultraviolet spectrum. *Opt Commun.* 2021;497:127182.
193. Banerji S, Sensale-Rodriguez B. Inverse designed achromatic flat lens operating in the ultraviolet. *OSA Continuum.* 2020;3(7):1917–29.
194. Kenney M, Grant J, Hao D, et al. Large area metasurface lenses in the NIR region. In: *Modeling aspects in optical metrology VII: SPIE;* 2019. p. 56–66.
195. Phan T, Sell D, Wang EW, et al. High-efficiency, large-area, topology-optimized metasurfaces. *Light: Sci App.* 2019;8(1):1–9.
196. Li Q, Wright JB, Chow WW, et al. Single-mode GaN nanowire lasers. *Opt Express.* 2012;20(16):17873–9.
197. Li C, Wright JB, Liu S, et al. Nonpolar InGaN/GaN core-shell single nanowire lasers. *Nano Lett.* 2017;17(2):1049–55.
198. Zhao D, Lin Z, Zhu W, et al. Recent advances in ultraviolet nanophotonics: from plasmonics and metamaterials to metasurfaces. *Nanophotonics.* 2021;10(9):2283–2308.
199. Byrnes SJ, Lenef A, Aieta F, et al. Designing large, high-efficiency, high-numerical-aperture, transmissive metalenses for visible light. *Opt Express.* 2016;24(5):5110–24.
200. Lin Z, Groeover B, Capasso F, et al. Topology-optimized multilayered metaoptics. *Phys Rev Appl.* 2018;9(4):044030.
201. Wang S, Wu PC, Su V-C, et al. Broadband achromatic optical metasurface devices. *Nat Commun.* 2017;8(1):1–9.
202. Hsiao HH, Chen YH, Lin RJ, et al. Integrated resonant unit of metasurfaces for broadband efficiency and phase manipulation. *Adv Optical Mat.* 2018;6(12):1800031.
203. Wang Y, Chen Q, Yang W, et al. High-efficiency broadband achromatic metalens for near-IR biological imaging window. *Nat Commun.* 2021;12(1):1–7.
204. Ndao A, Hsu L, Ha J, et al. Octave bandwidth photonic fishnet-achromatic-metalens. *Nat Commun.* 2020;11(1):1–6.
205. Arbabi E, Arbabi A, Kamali SM, et al. Controlling the sign of chromatic dispersion in diffractive optics with dielectric metasurfaces. *Optica.* 2017;4(6):625–32.
206. She A, Zhang S, Shian S, et al. Large area metalenses: design, characterization, and mass manufacturing. *Opt Express.* 2018;26(2):1573–85.
207. Arbabi A, Arbabi E, Kamali SM, et al. Miniature optical planar camera based on a wide-angle metasurface doublet corrected for monochromatic aberrations. *Nat Commun.* 2016;7(1):1–9.
208. Lassalle E, Mass TW, Eschimese D, et al. Imaging properties of large field-of-view quadratic metalenses and their applications to fingerprint detection. *Acs Photonics.* 2021;8(5):1457–68.
209. Monticone F, Valagiannopoulos CA, Alù A. Parity-time symmetric nonlocal metasurfaces: all-angle negative refraction and volumetric imaging. *Phys Rev X.* 2016;6(4):041018.
210. Pendry JB. Negative refraction makes a perfect lens. *Phys Rev Lett.* 2000;85(18):3966.
211. Xu T, Agrawal A, Abashin M, et al. All-angle negative refraction and active flat lensing of ultraviolet light. *Nature.* 2013;497(7450):470–4.
212. Kaina N, Lemoult F, Fink M, et al. Negative refractive index and acoustic superlens from multiple scattering in single negative metamaterials. *Nature.* 2015;525(7567):77–81.
213. Estakhri NM, Neder V, Knight MW, et al. Visible light, wide-angle graded metasurface for back reflection. *Acs Photonics.* 2017;4(2):228–35.
214. Aieta F, Genevet P, Kats M, et al. Aberrations of flat lenses and aplanatic metasurfaces. *Opt Express.* 2013;21(25):31530–9.
215. Martins A, Li K, Li J, et al. On metalenses with arbitrarily wide field of view. *Acs Photonics.* 2020;7(8):2073–9.
216. Chen C, Chen P, Xi J, et al. On-chip monolithic wide-angle field-of-view metalens based on quadratic phase profile. *AIP Adv.* 2020;10(11):115213.
217. Engelberg J, Zhou C, Mazurski N, et al. Near-IR wide-field-of-view Huygens metalens for outdoor imaging applications. *Nanophotonics.* 2020;9(2):361–70.
218. Pu M, Li X, Guo Y, et al. Nanoapertures with ordered rotations: symmetry transformation and wide-angle flat lensing. *Opt Express.* 2017;25(25):31471–7.
219. Park JS, Zhang S, She A, et al. All-glass, large metalens at visible wavelength using deep-ultraviolet projection lithography. *Nano Lett.* 2019;19(12):8673–82.
220. Zhang S, Kim MH, Aieta F, et al. High efficiency near diffraction-limited mid-infrared flat lenses based on metasurface reflectarrays. *Opt Express.* 2016;24(16):18024–34.
221. Roy T, Zhang S, Jung IW, et al. Dynamic metasurface lens based on MEMS technology. *Apl Photonics.* 2018;3(2):021302.
222. Hu T, Tseng C-K, Fu YH, et al. Demonstration of color display metasurfaces via immersion lithography on a 12-inch silicon wafer. *Opt Express.* 2018;26(15):19548–54.
223. Li N, Fu YH, Dong Y, et al. Large-area pixelated metasurface beam deflector on a 12-inch glass wafer for random point generation. *Nanophotonics.* 2019;8(10):1855–61.

224. Xu Z, Dong Y, Fu YH, et al. Embedded dielectric metasurface based subtractive color filter on a 300mm glass wafer. In: 2019 conference on lasers and electro-optics (CLEO): IEEE; 2019. p. 1–2.
225. Hu T, Zhong Q, Li N, et al. CMOS-compatible a-Si metalenses on a 12-inch glass wafer for fingerprint imaging. *Nanophotonics*. 2020;9(4):823–30.
226. Shalaginov MY, An S, Zhang Y, et al. Reconfigurable all-dielectric metalens with diffraction-limited performance. *Nat Commun*. 2021;12(1):1–8.
227. Cui Y, Zheng G, Chen M, et al. Reconfigurable continuous-zoom metalens in visible band. *Chin Opt Lett*. 2019;17(11):111603.
228. Afridi A, Canet-Ferrer J, Philippet L, et al. Electrically driven varifocal silicon metalens. *ACS Photonics*. 2018;5(11):4497–503.
229. He Q, Sun S, Zhou L. Tunable/reconfigurable metasurfaces: physics and applications. *Research*. 2019;2019:1849272.
230. Arbabi E, Arbabi A, Kamali SM, et al. MEMS-tunable dielectric metasurface lens. *Nat Commun*. 2018;9(1):1–9.
231. Papaioannou M, Plum E, Rogers ET, et al. All-optical dynamic focusing of light via coherent absorption in a plasmonic metasurface. *Light: Sci App*. 2018;7(3):17157.
232. Zhong JW, An N, Yi NB, et al. Broadband and tunable-focus flat lens with dielectric Metasurface. *Plasmonics*. 2016;11(2):537–41.
233. Ahmed R, Butt H. Strain-multiplex Metalens Array for tunable focusing and imaging. *Adv Sci*. 2021;8(4):2003394.
234. Elsayy MM, Gourdin A, Binois M, et al. Multiobjective statistical learning optimization of RGB metalens. *ACS Photon*. 2021;8(8):2498–508.
235. Yao K, Unni R, Zheng Y. Intelligent nanophotonics: merging photonics and artificial intelligence at the nanoscale. *Nanophotonics*. 2019;8(3):339–66.
236. Zhu M, Abdollahramezani S, Hemmatyar O, et al. Linear and nonlinear focusing using reconfigurable all-dielectric Metalens based on phase-change materials. In: *Laser science: Optical Society of America*; 2020. p. JW6B.
237. Schlickriede C, Kruk SS, Wang L, et al. Nonlinear imaging with all-dielectric metasurfaces. *Nano Lett*. 2020;20(6):4370–6.
238. Chen J, Wang K, Long H, et al. Tungsten disulfide–gold nanohole hybrid metasurfaces for nonlinear metalenses in the visible region. *Nano Lett*. 2018;18(2):1344–50.
239. Li L, Liu Z, Ren X, et al. Metalens-array–based high-dimensional and multiphoton quantum source. *Science*. 2020;368(6498):1487–90.
240. Almeida E, Shalem G, Prior Y. Subwavelength nonlinear phase control and anomalous phase matching in plasmonic metasurfaces. *Nat Commun*. 2016;7(1):1–7.
241. Gao Y, Fan Y, Wang Y, et al. Nonlinear holographic all-dielectric metasurfaces. *Nano Lett*. 2018;18(12):8054–61.
242. Andr n D, Mart nez-Llin s J, Tassin P, et al. Large-scale metasurfaces made by an exposed resist. *ACS Photon*. 2020;7(4):885–92.
243. Yoon G, Kim K, Huh D, et al. Single-step manufacturing of hierarchical dielectric metalens in the visible. *Nat Commun*. 2020;11(1):1–10.
244. Saha SK, Wang D, Nguyen VH, et al. Scalable submicrometer additive manufacturing. *Science*. 2019;366(6461):105–9.
245. Guo LJ. Nanoimprint lithography: methods and material requirements. *Adv Mater*. 2007;19(4):495–513.
246. Liu Z, Liu N, Schroers J. Nanofabrication through molding. *Prog Mater Sci*. 2022;125:100891.
247. Guo M, Qu Z, Min F, et al. Advanced unconventional techniques for sub-100 nm nanopatterning. *InfoMat*. 2022;4(8):e12323.
248. Sreenivasan S. Nanoimprint lithography steppers for volume fabrication of leading-edge semiconductor integrated circuits. *Microsyst Nanoeng*. 2017;3(1):1–19.
249. Stewart MD, Johnson SC, Sreenivasan SV, et al. Nanofabrication with step and flash imprint lithography. *J Micro/Nanolithography MEMS MOEMS*. 2005;4(1):011002.
250. Ganesan R, Dumond J, Saifullah MS, et al. Direct patterning of TiO<sub>2</sub> using step-and-flash imprint lithography. *ACS Nano*. 2012;6(2):1494–502.

## Publisher's Note

Springer Nature remains neutral with regard to jurisdictional claims in published maps and institutional affiliations.